LA-UR-15-23333
Approved for public release; distribution is unlimited.

Title: A Methodology for Calculating Radiation Signatures

Author(s): Klasky, Marc Louis
Wilcox, Trevor
Bathke, Charles G.
James, Michael R.

Intended for: Report

Issued: 2015-05-01

A Methodology for Calculating Radiation Signatures

Marc Klasky, Michael James, Trevor Wilcox, Chuck Bathke
Los Alamos National Laboratory
October 27, 2014

Table of Contents

Figures

Tables

Executive Summary

A rigorous formalism is presented for calculating radiation signatures from both Special Nuclear Material (SNM) as well as radiological sources. The use of MCNP6 in conjunction with CINDER/ORIGEN is described to allow for the determination of both neutron and photon leakages from objects of interest. In addition, a description of the use of MCNP6 to properly model the background neutron and photon sources is also presented. Examinations of the physics issues encountered in the modeling are investigated so as to allow for guidance in the user discerning the relevant physics to incorporate into general radiation signature calculations. Furthermore, examples are provided to assist in delineating the pertinent physics that must be accounted for. Finally, examples of detector modeling utilizing MCNP are provided along with a discussion on the generation of Receiver Operating Curves, which are the suggested means by which to determine detectability radiation signatures emanating from objects.

1.0 Introduction

The detection of concealed nuclear material is of paramount importance to the security of the United States. As such, the determination of the radiation signatures and optimization of the radiation detection architecture is a necessary step in designing systems to maximize the detectability of the radiation signatures and consequently reducing the likelihood of a nuclear event within the US. It is imperative to employ numerical simulations in designing and optimizing detection architectures because of the large ensemble of possible threat objects that may be of interest in detecting, wide-ranging environments that need to be assessed, a wide range of possible detection techniques (passive/active), numerous detectors and arrangements and detection algorithms, and neutron/gamma backgrounds.

The use of numerical simulation necessitates a formalism to ensure that both the pertinent physics is represented in the modeling and that benchmarking of results produces both reproducible and accurate representations of this complex problem. Furthermore, the simulation technique should be able to accommodate the proper modeling of a multitude of physics issues that are encountered in modeling radiation transport and subsequent detection of radiological sources. A recent review of the brightness methodology of Reference 1[1] and radiation signature calculations accompanying References 2-3[2,3] has identified issues that warrant further investigation. These issues are as follows:

- Appropriateness of 1-D representations of some objects
- Appropriateness of 1-D to model complex inherently 3-D scenes
- Use of group structure neutron cross sections
- Appropriateness of the photon scatter treatment
- Appropriateness of the exclusion of the background from the calculation of the source leakages
- Appropriateness of the brightness metric (non-inclusion of spectral effects) as a means to assess detectability
- Appropriateness of the equivalent shielding methodology[4] for multiplying media

This assessment led to the conclusion that a rigorous formalism is needed to properly delineate the pertinent physics models that are required to accurately simulate radiation signatures and that a more rigorous treatment of detectability is needed. Furthermore, because of the influence of the background and the impact that it may have in determining the detectability of radiological materials, we explore a means of detectability that can be made in the presence of background. In this report we present a methodology for properly modeling radiation signatures and detectability.

Arguably, MCNP has the most extensive benchmarking in both neutron and photon transport of any particle transport code and is viewed as the "gold standard."[5] An extensive amount of benchmarking of MCNP in the area of radiation signature and detector modeling has been previously performed.[6,7,8]Consequently, we employ MCNP6 as the means by which to perform the radiation signature simulations. MCNP6 is a general-purpose Monte Carlo code that can be used for transport modeling of coupled neutron, photon, and 34 other sub-atomic particles.[9] It also includes the background signal, which in some cases may appreciably contribute to the overall signal via induced fission.[10] Furthermore, additional capabilities recently added to MCNP allow for the generation of Receiver Operating Curves (ROC) to assess the detectability of objects.

A flow sheet of the methodology for computing radiation signatures is presented in Fig. 1. In the remainder of this report we present the modeling details for each of the respective elements of the simulation.

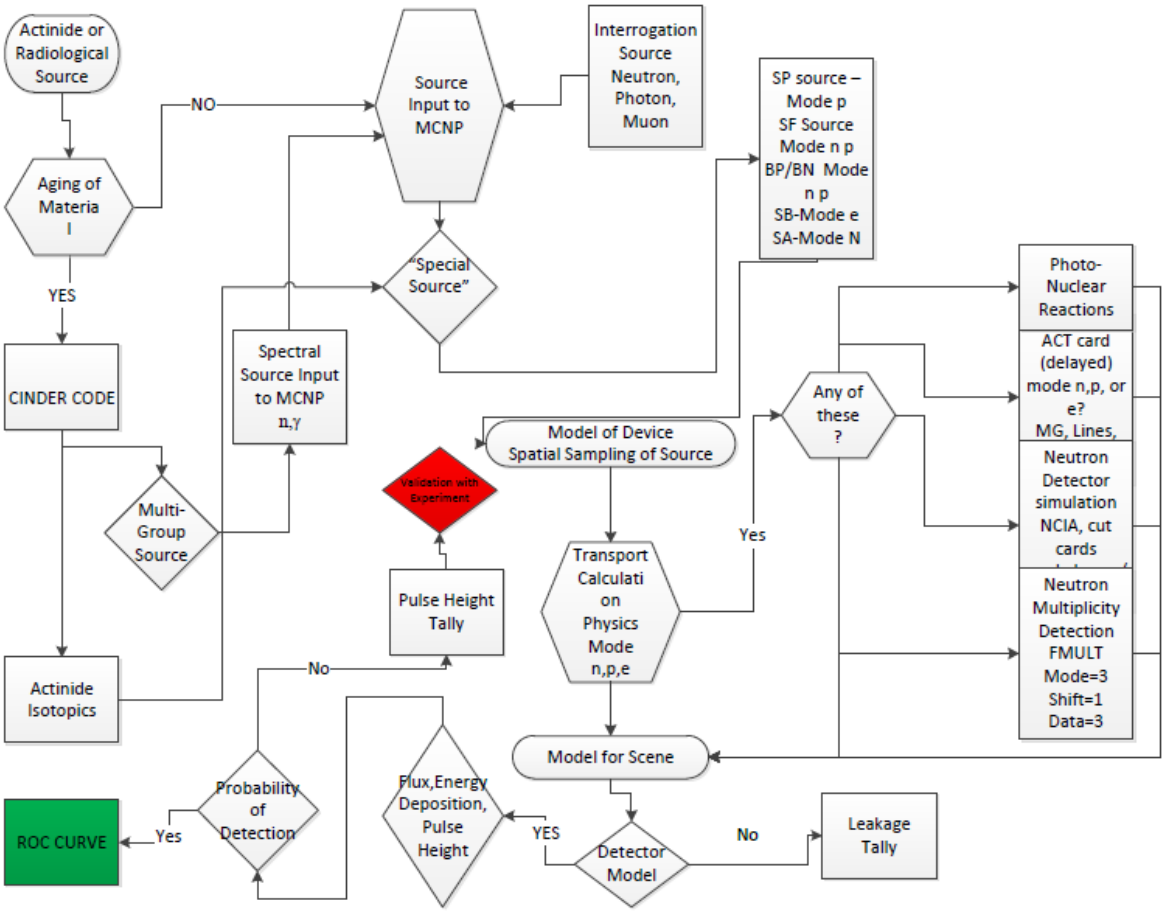

Fig. 1. Radiation Signature Flow Diagram

Fig. 1a. Continuation of Fig. 1

In Fig. 1 we have highlighted several features. First and foremost we have highlighted in red the necessity for the methodology to be benchmarked with experimental data. In addition, we have highlighted in green the Receiver Operating Curve because we believe that ultimately this is the best metric to assess the detectability of an object.

The intent of this document is twofold: 1) to describe details of the application of MCNP6 for determining radiation signatures, and 2) to examine the effect of various physics issues to identify the necessary and sufficient physics models to determine the detectability of radiological materials.

In Section 1.1 we provide a brief discussion of the numerous neutron and photon reactions that must be considered in determining the radiation signatures of radiological materials. Section 2 provides a discussion of the various sources and particle interactions to be evaluated prior to modeling the neutron and photon transport. More specifically, Section 2 includes details on both the intrinsic photon sources arising from α,β decay, spontaneous-fission-generated prompt and delayed neutron and photon sources, α,n sources, photon sources arising from beta particles, external neutron/photon sources, and finally neutron and photon backgrounds. In Section 3 we provide general guidance on basic issues associated with utilizing MCNP6 to calculate the photon and neutron leakages from objects. Several examples of neutron/photon leakage calculations are provided in Section 4. Section 5 provides some general remarks regarding the overall geometry and setting that the objects examined in Section 4 may be located, that is, scenes. The issues associated with the modeling of various neutron and photon detectors that may be utilized in detecting radiological sources and SNM are provided in Section 6. The issue of detectability and the calculation of ROC utilizing MCNP6 are provided in Section 7. Finally, in Section 8 we give conclusions and suggestions for future work.

1.1 Particles and Nuclear Reactions to Consider

In this section we briefly outline the nuclear reactions that need to be considered to determine the radiation signatures emanating from either Special Nuclear Material (SNM) or radioactive sources. In modeling the radiation signatures from either SNM or radiological sources, we are generally concerned with the detection of the neutrons and photons that arise from both the radioactive decay (α,β) of the material and the intrinsic spontaneous fission of the actinides. (It is

noted that the spontaneous fission process creates both neutrons and gammas.) We denote this radiation as the intrinsic source of the material and describe the modeling of this source in Section 2.1. In addition to the neutrons that are created by spontaneous fission of the actinides, an additional source of neutrons that is attributed to the interaction of the alpha particles with low-Z materials such as oxygen, fluorides, etc., may need to be incorporated into the source. This additional intrinsic source is described in Section 2.2.

As previously noted beta decay is one of the prominent decay mechanisms. The impact of the beta particle as an additional means by which additional radiation via bremsstrahlung radiation or annihilation radiation is presented in Section 2.3. In addition, numerous proposed active interrogation techniques utilize external forms of radiation to produce additional signal neutrons/photons that may facilitate the detection of SNM. These additional sources are briefly discussed in Section 2.4. Finally, as has been discussed in Reference 4 the background neutrons/photons created by cosmic rays provide a source that may create additional signal via the following two reactions:

- γ,n photo-fission in high Z materials
- n,f (induced fission)

These two additional mechanisms by which additional signal is generated are discussed in Section 2.5.

The neutrons that are produced via the aforementioned mechanisms may subsequently interact with the nuclei in the media by one of the following mechanisms:

- n,f
- n,n elastic
- n,n' inelastic
- n,γ radiative capture
- (n,2n),(n,xn)

A discussion of the neutron transport of the source neutrons and the various neutron interaction mechanisms is provided in Section 3.

The transport of photons arising from both α,β decay of SNM as well as the decay of radioisotopes (delay photons) is another important aspect of determining radiation signatures. During the transport through the media the photons may interact in a variety of ways including:

- Nuclear Resonance Fluorescence
- Photo-neutron
- Photoelectric Effect
- Bremsstrahlung
- Compton Scatter

- Coherent Scatter
- Pair Production
- Annihilation Radiation
- Auger Electron Generation

Additional discussion of these photon interaction mechanisms is provided in Section 3.

2.0 Source Modeling Sections

In Fig. 1, the specification of the intrinsic source is the first step in modeling the radiation signatures emanating from an object containing SNM or a radioactive source. Consequently, we first define the source geometry. An example of a very simplified geometry is given in Fig. 2.

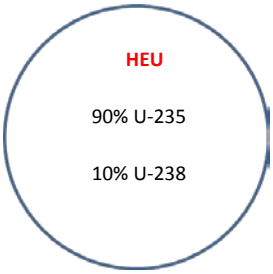

Fig. 2. HEU Object

Figure 2 represents SNM in a geometry that we denote as an object. In typical transport modeling we would simply specify the material characteristics and the geometry. A coupled neutron-photon calculation would then be performed to transport neutrons/photons to determine quantities such as the neutron multiplicity, the neutron leakage, and the photon leakage from the object. (These particles may then be transported through the object to a detector that is located within a scene.) Figure 3 presents such a configuration.

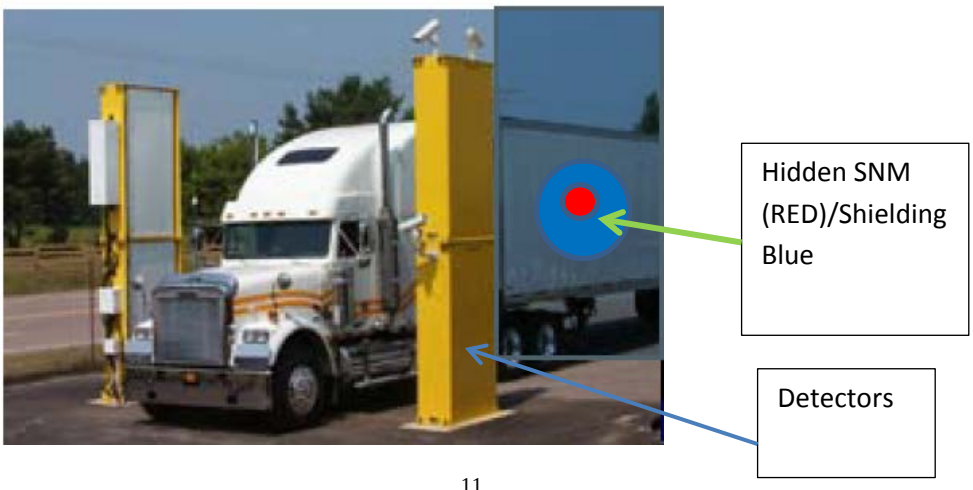

Fig. 3. SNM Object in Scene[11]

Before we can transport particles we must first determine the intrinsic source of both neutrons and photons that may be present during the counting period. The intrinsic source of the material is attributed to both the decay of the actinides α,β (and accompanying radiation emission) as well as the spontaneous fission process. Before discussing each of these respective decay mechanisms, we first must specify several quantities, in addition to the material composition of the SNM. These quantities are presented in Fig. 4.

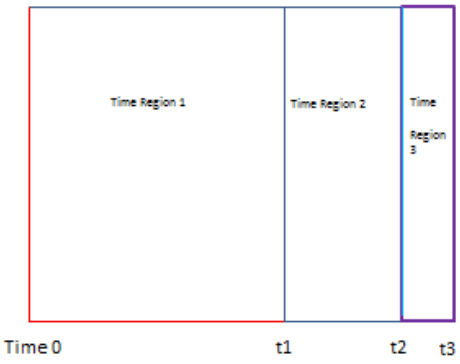

Fig. 4. Time Domain of the Source Calculation

Examination of Fig. 4 indicates that we have divided the specification of the source into three distinct pieces. The first region is from the initial specified composition of the SNM up to the time, t1, in which the material is placed into an object configuration, such as the one specified in Fig. 2. Prior to this time we assume that the SNM is in a very low reactivity configuration such that the multiplicity of the material is essentially unity. Following the placement of the SNM into a configuration in which the neutron multiplicity of the SNM is non-negligible, the SNM undergoes additional "aging" until time t2. Time t2 to t3 represent the time that the radiation emanating from the device is measured. We denote this time period as the "counting period." To properly specify the intrinsic source during the counting period, we must specify times t1, t2, and t3 in addition to the initial SNM isotopics and geometric configuration. As previously discussed, if the object of interest containing the SNM is contained within any shielding that may affect the multiplicity, it must be modeled to properly capture the coupling to the source.

In the following sections, we describe the details of the intrinsic source modeling in each of the respective time regions and the specification of the collective source to be utilized in the subsequent neutron/photon transport calculation.

2.1 Intrinsic Source due to Alpha and Beta Decay

Actinides undergo several decay mechanisms, most notably β^- and alpha decay. These decay mechanisms occur with constant half-lives and result in series of subsequent decays with accompanying gamma radiation emission due to the fact that many of the decay products are in

excited states. In this section we provide details modeling the intrinsic source attributed to the SNM due to both α,β and accompanying gamma emission.

Because α,β decay is independent of the material configuration, the source provided by α,β and accompanying gamma emission may be calculated using either CINDER[12] or ORIGEN[13] for the time 0 to t2. These codes solve or simulate the Bateman equation, which describes the radioactive decay process and in so doing determines the isotopic composition of each of the decay products at a specified time. The photon emission rates may then be determined by post-processing these results to determine the spectral intensity of the line emissions at a specified time. This post-processing of the isotopic composition of the decay products is performed either using the post-processing provided by CINDER or by using user-generated post-processing software using, for example, the decay database libraries at http//www.nndc.bnl.gov/nndcscr.[14]

The decay source obtained may then be used as a distributed source for the ensuing transport calculation, during the period t3-t2, within the SNM properly weighted using the MCNP Rad and SI cards that define the radial extent and spatial distribution of the source. To uniformly distribute the decay photon source arising from α,β decay we specify the radius with the rad card and use the SI card settings as -21 2 to uniformly distribute the material within the spherical geometry depicted in Fig. 2.

To illustrate the intrinsic source arising from α,β decay from HEU, initial composition specified in Table 1, Fig. 5 presents the photon intensities as a function of energy following 15 years of aging using ORIGEN. This composition is as representative HEU system without impurities. (Final isotopic compositions i.e. after aging are provided in Table 2.)

Table 1. Initial HEU Composition

Isotope	Weight Percent
U234	0.82
U235	93.5
U238	5.68

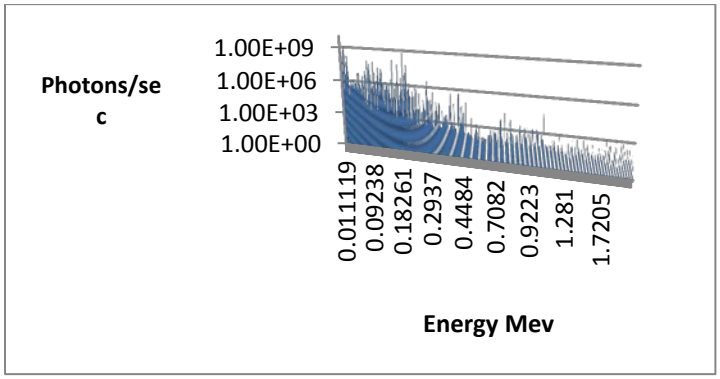

Fig. 5. Photon Intensities versus Energy HEU 15 Years Aging

Table 2. Isotopic Composition of HEU following 15 years of aging

88223	2.57647E-15
90227	4.24118E-15
90230	5.01176E-08
90231	3.82176E-12
90234	8.52941E-13
91231	1.36471E-08
92234	0.0012
92235	0.94
92238	0.588

The aging example presented above is a simple illustration of the calculation of the isotopic composition of an initial specified composition.

2.2 Intrinsic Source Due to Spontaneous Fission

In this section we describe the source modeling attributed to the intrinsic spontaneous fission source of the SNM. In addition to the previous decay modes, actinides decay via spontaneous fission and emit a number of neutrons, average number $\bar{\nu}$, and accompanying fission products. (Due to the short time frame in which the neutrons are emitted both due to prompt and delayed mechanisms (all within <1 minute) the neutron source, prompt and delayed, generated prior to the counting period is not needed in defining the source for all but the period t2-t3.) These accompanying fission products are excessively neutron rich and consequently decay through a sequence of β^- decays with accompanying γ rays. The computation of the photon source due to spontaneous fission is computed by first noting from Fig. 4 that we are dealing with three distinct regions in time over which spontaneous fission occur and fission products are generated.

In Region 1 of Fig. 4, the SNM is assumed to be in an infinitely dilute configuration such that the multiplicity of the system is close to unity, i.e., $\frac{1}{1-k_{eff}} \sim 1$. The spontaneous fission photon source after aging may be computed in this regime by one of the following methods:

1. By using CINDER and the accompanying post-processing to obtain a coarse 25 group photon source for the specified “aging” process. (It should be noted that ORIGEN currently does not provide for the photons that are emitted via spontaneous fission.) The use of the 25 group structure to capture the fission product photon emission is supported by quasi-continuum of lines above 1 MeV.
2. By using CINDER to obtain the fission product isotopics following the specified “aging” process and then generating the photon source utilizing the decay libraries to determine the photon emission spectra.

Due to the very large number of fission products that may be generated, we recommend that the processing of the constituent isotopes attributed to fission products be obtained using the post-processing capability of CINDER, 25 group representation. It should also be noted that the radiation detector that is employed also has a bearing the spectral resolution of the specified

source in that if HPGe detectors are utilized then specification of a fine energy binning structure may be necessary to match the experimental measurement whereas if in the more common portal detection architectures PVT detectors are utilized a coarse binning structure may be appropriate due to the inability of the PVT to identify lines. In the majority of the transport calculations presented in this report we presume that a course energy binning is appropriate due to the assumption of the use of PVT detectors.

Note: The instantaneous sources obtained using the methods above must be processed for the subsequent time period in which the counting is performed as discussed below. In addition, the prompt photons emitted during the spontaneous fission should be neglected for all time intervals except those in which counting are performed. (Additional discussion on this aspect of the delayed photon source is provided in Sections 2.2.1–3.)

In determining the decay photons that arrive in the counting window that is attributed to spontaneous fission occurring in Regions 1–2, Fig. 4, we must examine the time emission spectra of the delayed photons from spontaneous fission. To perform this task we use the following approach, as currently the specification of the spontaneous fission source does not have accompanying delayed photons, an approximation is made in which thermal neutrons are utilized to induce fission in a small sample of SNM. That is, the fission product yields are generated by the induced fission.

Note: We obtain the normalization, i.e., total decay photons/SF emitted over all time, by computing the ratio of photons created via neutrons to those induced via fission, i.e., loss to fission.

To generate the delayed photons from the thermal neutrons we utilize the following MCNP cards

SDEF ERG=2.54e-8

ACT FISSION=N P DG=MG

Note: The DG=MG option on the ACT card should be used unless specific line data is desired. In addition, to isolate the delayed photons from induced fission we omit the fmult method=5 card.

The appropriate spatial distribution of the source is again obtained through the use of the RAD and SP cards. We also provide time binning to capture the temporal distribution of the decay photons through the use of the t tally card.

As an illustration we present the temporal distribution of decay photons emitted by the induced thermal fission of HEU 100% U-235. The time distributions are presented in Figs. 6–10.

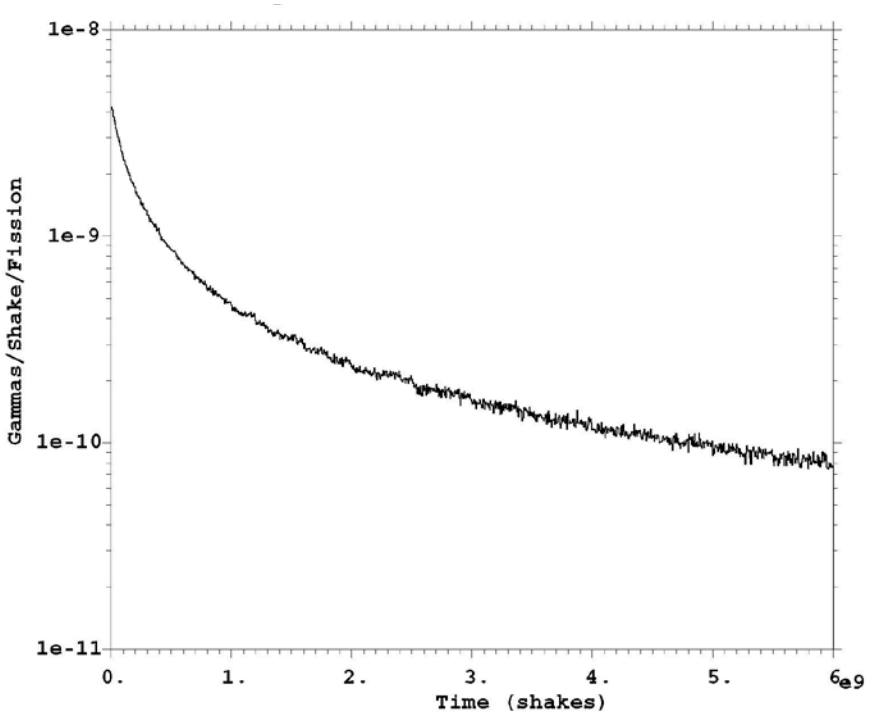

Fig. 6. Delayed gammas from 10 sh to 60 sec from Thermal Neutron Induced Fission

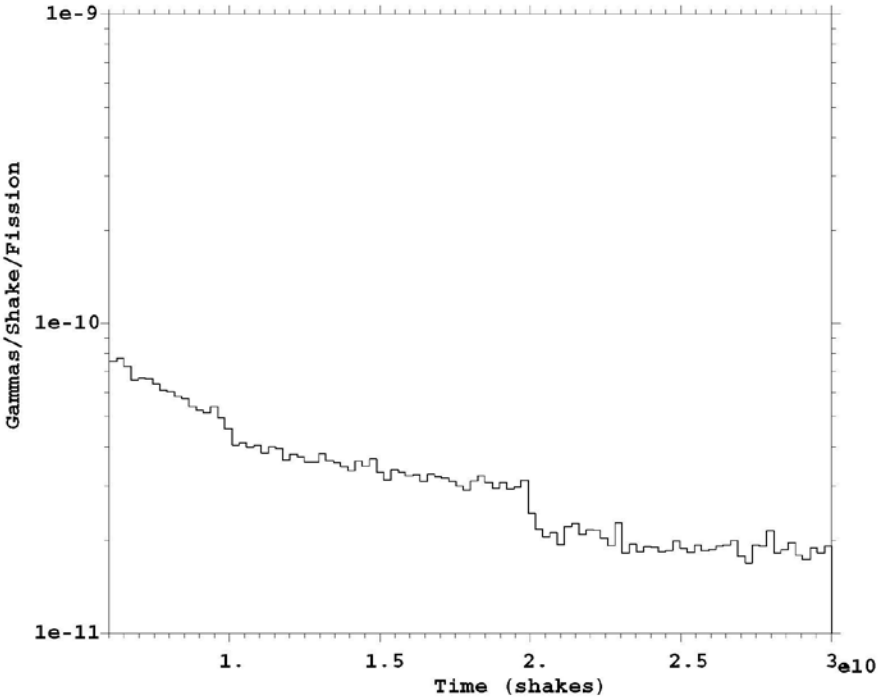

Fig. 7. Delayed Gammas from 60 sec to 5 min from Thermal Neutron Induced Fission

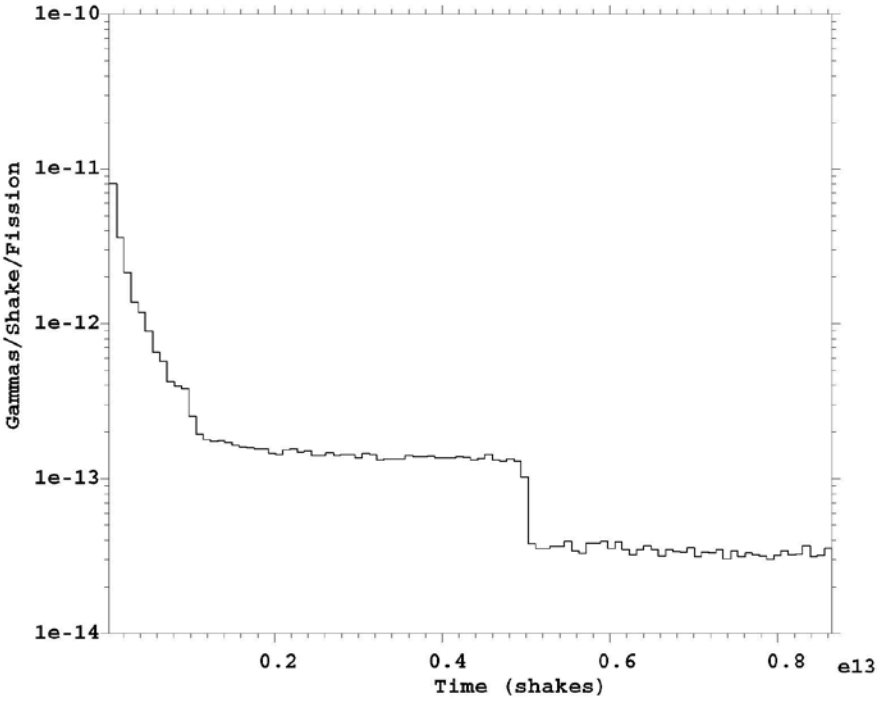

Fig. 8. Delayed Gammas from 5 min to 1 day from Thermal Neutron Induced Fission

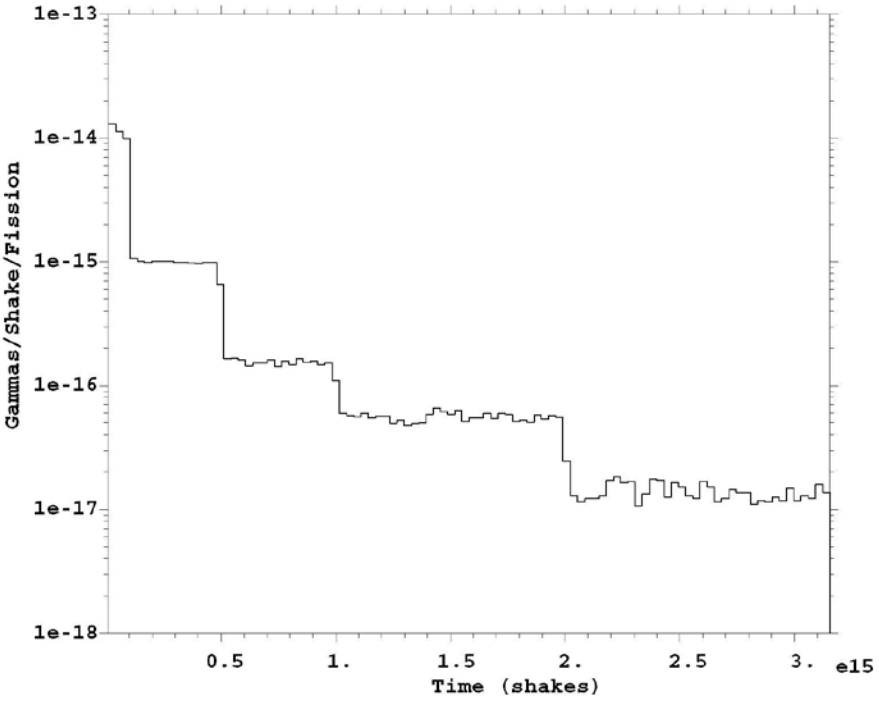

Fig. 9. Delayed Gammas from 1 day to 1 year from Thermal Neutron Induced Fission

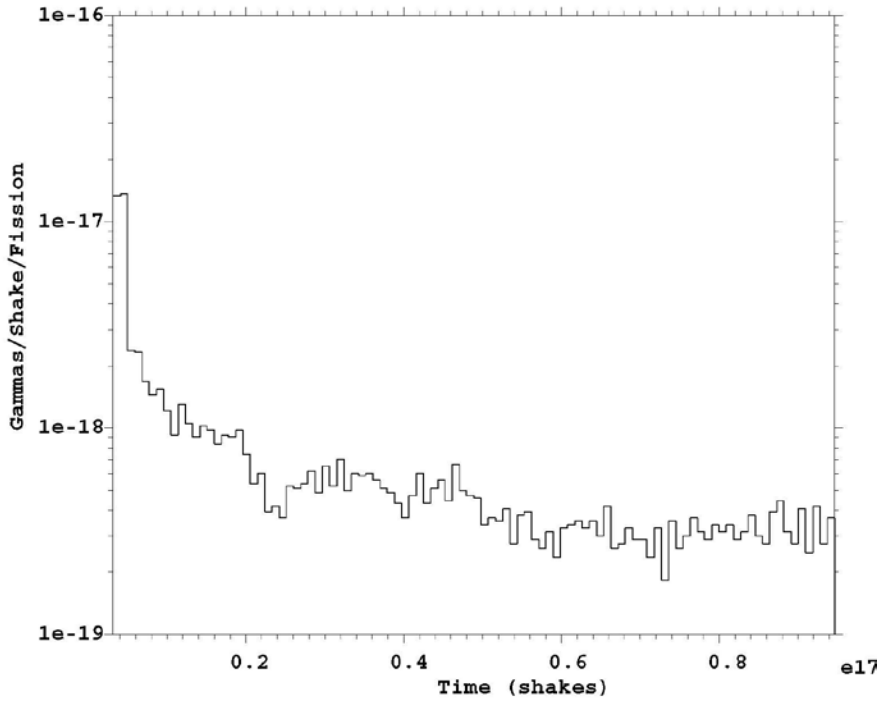

Fig. 10. Delayed Gammas from 1 year to 30 years from Thermal Neutron Induced Fission

Examination of Figures 6–10 indicates that a very large fraction of the photons are emitted within a short period following a spontaneous fission. That is, within the period of approximately a week almost 90% of the photons are emitted. To further illustrate this point a cumulative distribution of the fraction of photons emitted versus time is presented in Fig. 11.

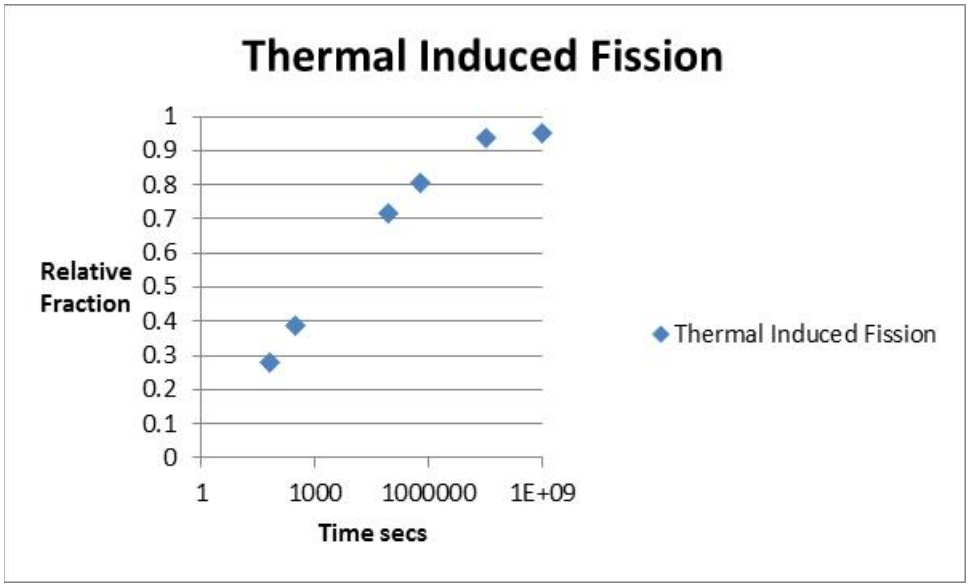

Fig. 11. Cumulative Fraction of Delayed Photons versus Time (Thermal Induced Fission)

The implication of the large majority of photons being emitted within a very short time period following a spontaneous fission is important in that if a sufficient time period between the spontaneous fission and the counting period is present, such is the typical case, i.e., t2-t1>>1 week, then the spontaneous fission source may be neglected.

In Figures 6–11 we have presented the details of the temporal distribution of emitted photons following a thermally induced fission. As previously discussed we have used a thermal neutron with energy 0.0254 eV to induce fission and then subsequently generate delay photons via the decay of the fission products. In systems with somewhat larger reactivity the production of fission products will be dominated by the induced fissions which may have energies more closely represented by the neutron energy of the spontaneous neutron distribution. The consequence of using this assumption with respect to the fission product production and the corresponding temporal distribution of delayed photon emissions may be compared to the previous assumption with respect to the energy of the induced fission in Fig. 12.

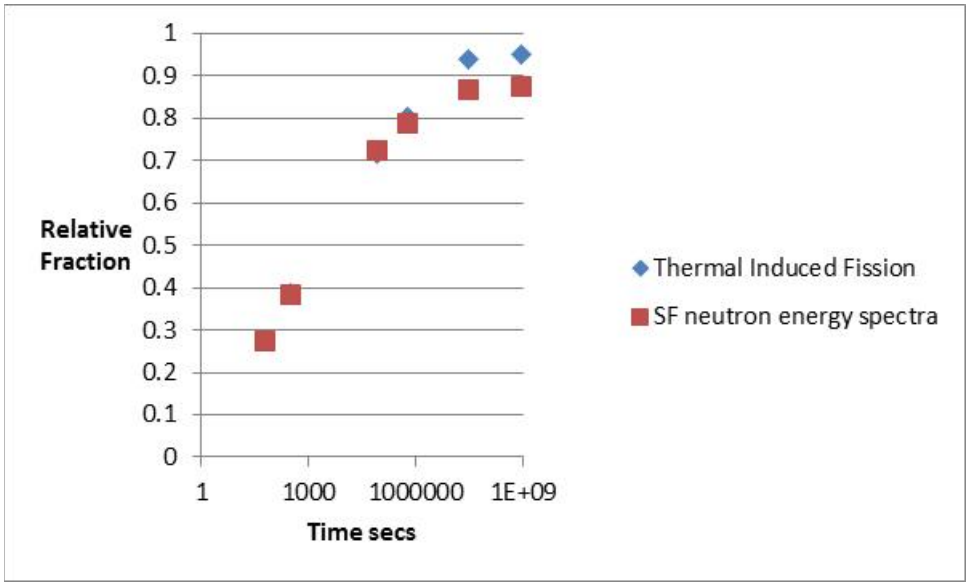

Fig. 12. Comparison of Cumulative Fraction of Delayed Photons versus Time

Note: In the time frame given by Region 2 where the SNM is assumed to be in a configuration in which multiplicity is such that the number of fissions by induced fission exceeds that of the spontaneous fission, we will use the spontaneous fission source neutron energy distribution to induce fissions in the small quantity of SNM as above.

In the subsequent discussion of the delayed photons emitted as a result of spontaneous fission we describe the time dependence of the decay photons arising from the decay of the accompanying fission products from spontaneous fission process as SFD (t), where SFD (t) has the temporal distribution as depicted in Figures 6–10.

2.2.1. Intrinsic Source due to Spontaneous Fission in Time Region 1

To facilitate the development of a mathematical model of the photons counted during the period t2 to t3 via the spontaneous fissions that occur during the time period 0 to t1 we present Fig. 13.

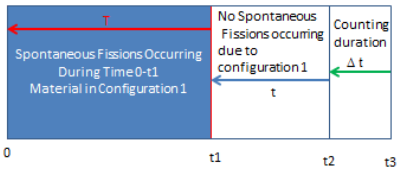

Fig. 13. Source Contributions from Time Region 1

In Fig. 13 we highlight the spontaneous photons that are emitted while the material is in the infinitely dilute configuration that is preceded by the configuration depicted in Fig. 2. Configuration 1 is assumed to persist for a time period t2-t1. Following time increment t, it is assumed that a counting period exists in which the signal emanating from the object is obtained. This counting period is assumed to occur in time increment t3-t2, or Δt in Fig. 13. By considering a time element ds within the time in which the spontaneous fission occurs namely 0 to t1, we may write an expression for the contribution of the source measured in the counting period Δt from the spontaneous fission occurring in the time window 0 to t1 as:

$$Source(0-t1) \cong SFR * \int_{t}^{t+T} SFD(s)ds \int_{0}^{\Delta t} dt \qquad \text{Equation 1}$$

Where:

$$SFR = SF/\sec gram * Mass\ SNM^{*}\#\text{Delay Photons/SF}$$

Note: Using our previously described method to determine the delayed photons from a spontaneous fission we have determined that the total number of delayed photons emitted is approximately 7.78/SF for HEU.

SFD(s) may be observed to fall off as a pseudo-exponential function in which the time is registered as zero at the time corresponding to the onset of counting and increases to the left in Fig. 13. Consequently, if there is a period t2-t1 that is on the order of months and the aging time is on the order of years, we observe from Figs. 6–10 that the contribution of the source from Region 1 that arises in the counting window is a very small fraction of the total delayed spontaneous photon source.

Note: In the derivation of Equation 1 we have assumed that the rate of emission at a relatively long time following the last spontaneous fission and the counting time has occurred such that the emission rate is constant over the counting period.

An alternative approach to compute the photon source due to spontaneous fission from occurring from time zero to t1, which is counted between times t2 and t3, is to utilize the photon source

due to spontaneous fission as given by CINDER at time t1 and then compute the number of photons that are emitted in the time window Δt. Mathematically we have:

$$SF_{Cinder(t1)} * f(\Delta t) \qquad \text{Equation 2}$$

Where:

$$SF_{Cinder(t1)} = \#\gamma/\sec at\ time\ t1$$

$$f(\Delta t) = fraction\ of\ photons\ from\ time\ t1\ arriving\ in\ the\ time\ window\ \Delta t$$

We note that an expression for $f(\Delta t)$ is given by $\frac{\int_{t2}^{t3} SFD(s)ds}{\int_{0}^{\infty} SFD(s)ds}$

Finally, we again emphasize that if we assume that there is a significant time between the last fission and the counting time and that the counting time is short, i.e., t3-t2 is much less than the total time from t1 to t3, then the contribution to the source due to the fissions created in time Region 1 will be negligible as may be seen from examining Figs. 6–10.

2.2.2 Intrinsic Source Due to Spontaneous Fission in Time Region 2

In a similar manner we may develop an expression for the contribution of the source attributed to the material when the material is in the configuration depicted in Fig. 2. Conceptually the source contribution from this region is exactly analogous to the previous source except that as previously discussed the source is amplified by the multiplicity of the system. (There is of course a difference in the times in which the spontaneous photons are emitted and the incremental increase in the fission products due to the additional aging.) Accordingly, we calculate the photon source determined in the infinitely dilute case and scale the infinitely dilute source by:$\frac{1}{1-keff}$. (It should be mentioned that the multiplication should be obtained via a source calculation and not an eigenvalue calculation due to the fact that the eigenvalue calculation implicitly assumes a critical system and the fundamental mode for the neutron flux profile.) A corresponding depiction of the contribution of the source arising from this configuration which persists in duration t1 to t2 and is counted from times t2 to t3 is presented in Fig. 14.

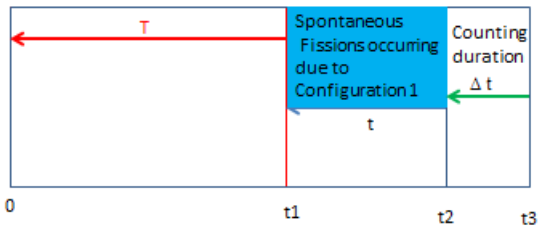

Fig. 14. Source Contributions from Time Region 2

In this case there is no effective delay time between the last spontaneous fission and the beginning of the counting period. Consequently, t2=0 and mathematically we represent the source contribution from this time period and configuration as:

$$SFR * \frac{1}{1-k_{eff}} \sum_{s=0^-}^{\Delta t} \int_0^t SFD(s+t)dt \qquad \text{Equation 3}$$

The expression above for the delayed source generated via spontaneous fission in Region 2 that are counted in Region 3 involves the integration over the time in which the source is generated namely from the time at which the detection begins 0^- and extends backwards in time to the onset of the source, i.e., t1. The 0^- time is just prior to the counting period and as such does not include the prompt photons emitted. The prompt neutrons emitted at 0^+ and throughout the counting period will be incorporated in the final source contribution term. The summation is utilized to account for the contribution of the source over the counting period extending from zero to Δt.

2.2.3 Intrinsic Source Due to Spontaneous Fission in Time Region 3

Finally, we examine the final time period in which the counting of particles, i.e., signal, occurs. In this region the source is emitted concurrent with the counting process. This region is depicted in Fig. 15.

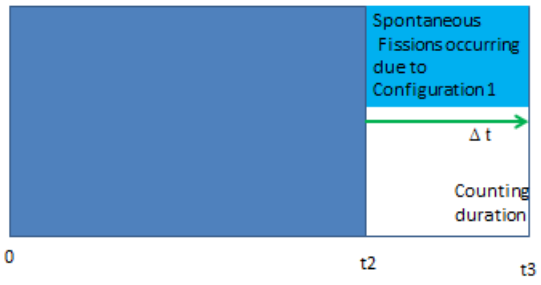

Fig. 15. Source Contributions from Time Region 3

An expression for the source may be developed and is given by:

$$\text{SFP}*\frac{1}{1-k_{eff}} * \Delta t + SFR * \frac{1}{1-k_{eff}} \sum_{i=0}^{\Delta t} \int_i^{\Delta t} SFD(t+i)dt \qquad \text{Equation 4}$$

Where:

$$SFP \equiv Prompt\ Photons$$

Note: To implement the prompt fissions from spontaneous fission the following MCNP code option must be utilized:

fmult method=5

As an example of the prompt photons generated via spontaneous fission we consider an infinitesimal sphere, i.e., radius $1*10^{-6}$ cm of HEU with composition specified in Table 1. The energy distribution of the prompt photons is given in Fig. 16.

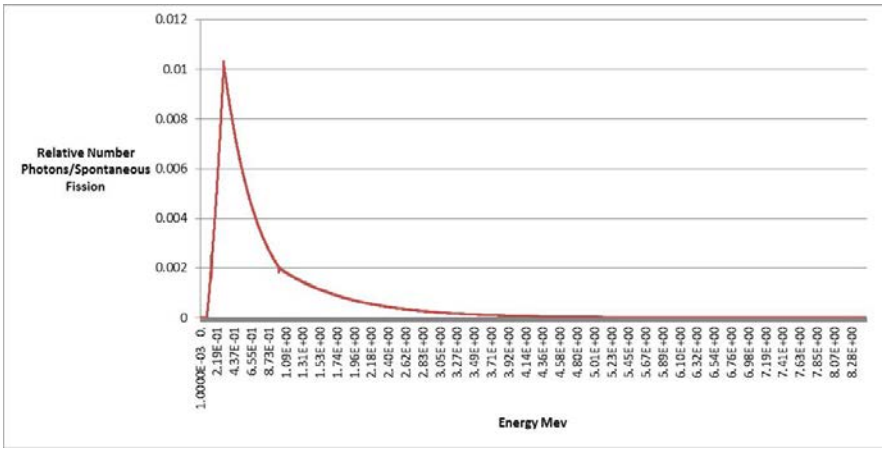

Fig. 16. Energy Distribution of Prompt Photons from Spontaneous Fission of HEU

The source for the previous example was generated with the following MCNP cards:

sdef par=-sf rad=d1

si1 0 0.000001

sp1 -21

The total number of prompt photons was calculated to be approximately 6.44.

Finally, we remark that to capture the entire intrinsic source that is counted in Region 3, we include the decay photons as discussed in Section 2.2.1 from the CINDER calculation which includes not only the decays photons accompanying α,β decay but also the decay photons that accompany spontaneous fission attributed to the fission products. To account for the prompt and delay photons (from induced fission), we utilize a spontaneous fission source (-SF) and specify the prompt photons from both spontaneous fission as well as induced fission with the following cards:

fmult method=5

The delayed photons emitted during the counting window and from the prior region, Region 2, are both captured by using the following MCNP card:

ACT FISSION=N P DG=MG

The multiplicity of the system is inherently captured via the neutron transport mode n by virtue of the introduction of the spontaneous neutron source.

2.3 Intrinsic Source Examples

In this section we present two examples to illustrate the effect of aging on the intrinsic source strength. In the first case we age HEU consisting of 90% atom U-235 and 8.3% atom U-238, 1.21%at U-234, and 0.38%at U-236. Figure 17 presents the aging calculation performed with CINDER and post-processed with a coarse 25 group energy group structure to obtain the photon intensities from both α,β and spontaneous fission.

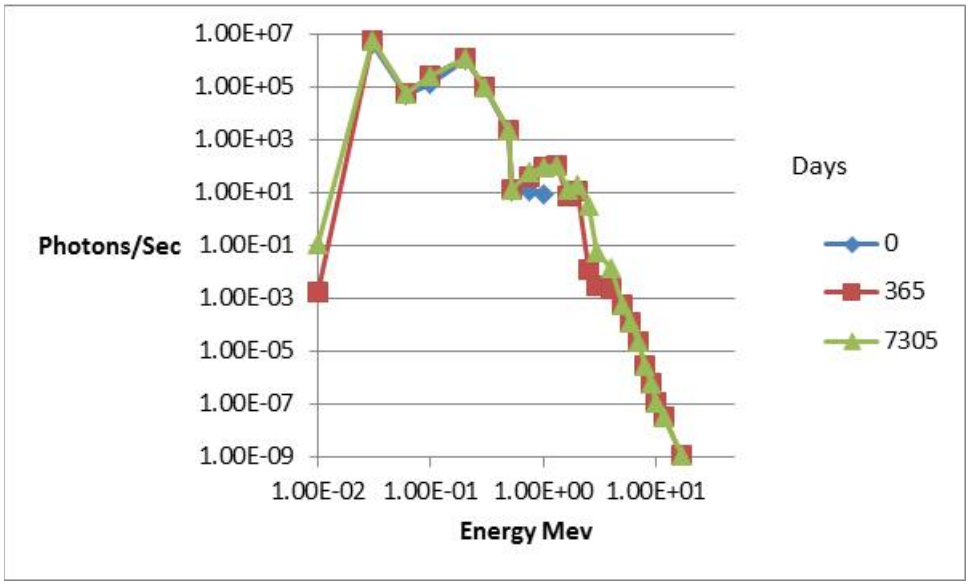

Fig. 17. HEU Aging Calculation Photons/sec versus Energy

Examination of Fig. 17 reveals that the gamma spectra for the three aged times are virtually identical below the upper emission line of Pa-234m. However, during the aging process fission products are accumulated such that there is a general buildup of activity above the upper emission line of Pa-234m. Further examination of Fig. 17 reveals that the fission products emission rate is less than six orders of magnitude than the approximately hundred keV photons in magnitude. However the hundred keV photons are much more readily attenuated than the multi-MeV photons and consequently the effect of shielding will be to dramatically reduce the magnitude of the lower 100 keV photons.[15] In the limit of very thick shielding the magnitudes of the emissions via the fission products can approach the decay photons. (It should be noted that the efficiency of detecting these high energy photons is lower than the lower energy photons.)

Fig. 18 presents an analogous CINDER aging calculation for weapons grade plutonium consisting of Pu-238 5.95e-3 atom%, Pu-239 96.233 atom%, Pu-240 3.63atom%, Pu-241 0.13 atom%, and Pu-242 4.6e-3 atom%.

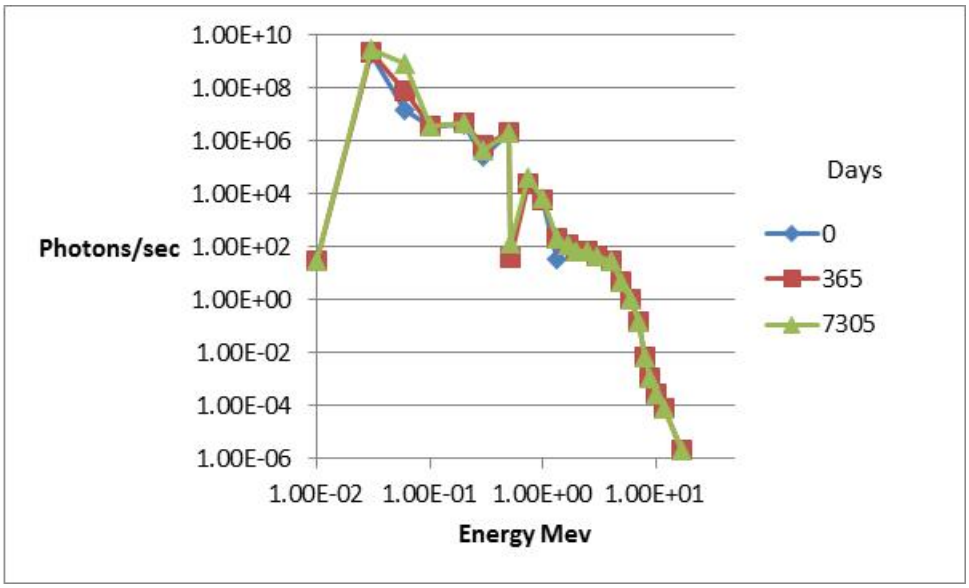

Fig. 18. Pu-W Aging Calculations Photons versus Energy

Examination of Fig. 18 indicates that unlike the HEU, aging of plutonium dramatically increases the emission of photons below the upper decay lines of plutonium, i.e., ~1 MeV. This effect is apparent in viewing Fig. 18 in the ~60 keV range. This increase in emission is attributed to the buildup of Am-241. Finally, the aging of plutonium again produces fission products whose decay gammas exceed the highest energy decay line of plutonium.

2.4 α,n Source

The radioactive decay of the actinides may proceed via alpha decay. These energetic alpha particles may subsequently interact with low Z materials and through the α,n reaction release a neutron. The determination of the source attributed to the production of neutrons via this mechanism may be calculated with the SOURCES code.[16] The SOURCES code is a computer code that determines the neutron production rates and spectra from α,n spontaneous fission, and delayed neutron emission due to the decay of radionuclides. This source may then be uniformly distributed within the SNM during a coupled neutron/photon transport MCNP6 calculation to determine the neutron and photon leakages from the object during the t2-t3 time frame.

Figure 19 presents a comparison between experimental data and the use of the SOURCES code and the SOURCES/MCNP simulation in which the neutrons with energy spectra calculated with SOURCES was utilized as the source in an MCNP calculation.

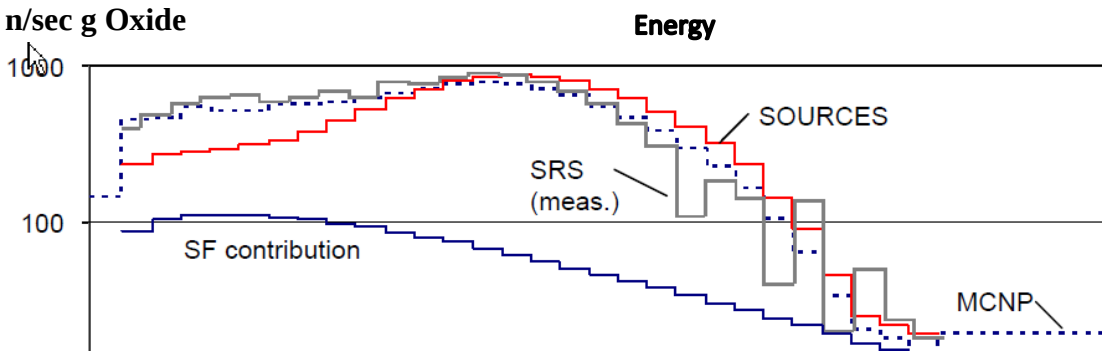

Fig. 19. SOURCES-SOURCES/MCNP-Experimental PuO_2 neutron spectra[17]

An alternative to using the SOURCES code is to use MCNP6 and specify SA as an additional source using the SDEF card with the par=SA option. However, the libraries required for this computation have not been distributed with the code and need to be acquired through http://www.talys.eu/contact/.[18] Furthermore, benchmarking of the (α,n) reaction is needed prior to use.

2.5 Beta Particle Source

As previously discussed one of the decay modes of the actinides and fission products is through β decay. In this process the unstable nucleus emits an electron. This beta particle may subsequently interact with the Coulomb field of the electrons, in the presence of a nucleus, and create Bremsstrahlung radiation. We may compute the accompanying source that may be generated by β decay by invoking the MCNP ACT card with the NONFISSION=e and Fission= e options. In addition, we specify electron transport on the MODE card. It should be noted that β particles will only be produced via decay due to the fission products that are produced and decay through this mechanism, i.e., PAR=SP. If the intent is to examine the direct contribution of beta decay from, for example, an actinide, we may utilize the PAR=d2 card (to specify a distribution) and include SB along with SP on the PAR card. Alternatively, if a source neutron is specified by, for example, PAR=-SF, specification of FISSION=p n e NONFISSION=p n e on the ACT card will produce delay neutrons, photons, and beta particles. (Transport of the electrons is specified on the MODE card with e.)

We have examined the impact of beta decay by comparing the photon current at the boundary of a 15-year aged HEU system. The isotopics after 15 years are given in Table 2. A comparison of the photon current at the boundary indicates that the photon current given by the SB source is negligible in comparison with the SP source. Consequently, we conclude that the effect of β decay on the photon current is negligible and can be neglected.

2.6 External Neutron/Photon Sources

The detection of SNM may be performed either utilizing active or passive techniques. Table 3 presents a number of active interrogation techniques that have been proposed for use in detecting SNM.[19]

Table 3. Active Interrogation Techniques[20]

Technique	Presence	Enrichment	Mass	Interrogation Source	Strengths / Limitations
Gamma spectroscopy	Y	Y	N	None	Small quantities of bare HEU can be detected in seconds. Low-energy gamma rays are easily shielded.
Neutron multiplicity	Y	N	N	None	Neutron detection is viable when gammas are shielded. The spontaneous fission rate is extremely low, requiring large quantities of HEU, very long count times, optimal detector configurations, and low neutron backgrounds.
Differential die-away (DDA) analysis	Y	N	N	Neutrons or Photons	Small HEU samples on the order of grams can be detected. Specificity is less than for gamma techniques, and the DDA signature can be easily eliminated with neutron poisons.
Neutron multiplicity	Y	N	Y	Neutrons or Photons	Induced fission neutrons penetrate high-Z shielding. The presence of ^{235}U is inferred by neutron multiplication.
Fission, beta-delayed gamma spectroscopy	Y	Y	N	Neutrons or Photons	Delayed gammas have a higher energy than passive gammas. Measurement times are long to build up fission fragments.
Fission, beta-delayed neutrons	Y	Y	Y	Neutrons or Photons	Detects gram quantities of HEU, even in shielding. Specificity is less than for gamma techniques, and delayed neutrons are lower in energy than fission neutrons and are more easily attenuated.
Prompt-gamma spectroscopy	Y	Y	N	Thermal Neutrons	Uranium-235 prompt gamma energies are high enough to escape most items. Some study is needed on required source intensity.
Fast neutron imaging	Y	Y	Y	API Neutron Generator	Imaging can locate HEU. Measurement times tend to be long.
Prompt fission neutron energy discrimination	Y	N	N	Neutrons or Photons	High-energy neutrons from fission are distinct and easily detected. Neutron moderators quickly decrease neutron energies below the detection threshold.
Nuclear resonance fluorescence	Y	Y	N	Photons	Good specificity to ^{235}U. Thick targets are very difficult to measure because of the attenuation of ingoing and outgoing photons/gammas and Compton scattering.
X-ray imaging	Y	N	N	X-Ray Source	Good for detecting high-Z shielding. Image interpretation can be complicated.
Muon imaging	Y	N	N	Cosmic-Ray Muons	Uses the cosmic-ray background. Effective density-based material compounds and measurement times tend to be long.

Modeling of these proposed active interrogation techniques may be easily accomplished using MCNP6 by specifying the characteristics of the source neutrons/photons/muons on the source definition card. Furthermore, spectral/temporal and angular specifications of the source may also be easily incorporated into the source definition card. Finally, the intrinsic source characteristics

may also be simultaneously incorporated. An example of an active interrogation technique utilizing high-energy photons to induce photo-fission is depicted in Fig. 20.[21]

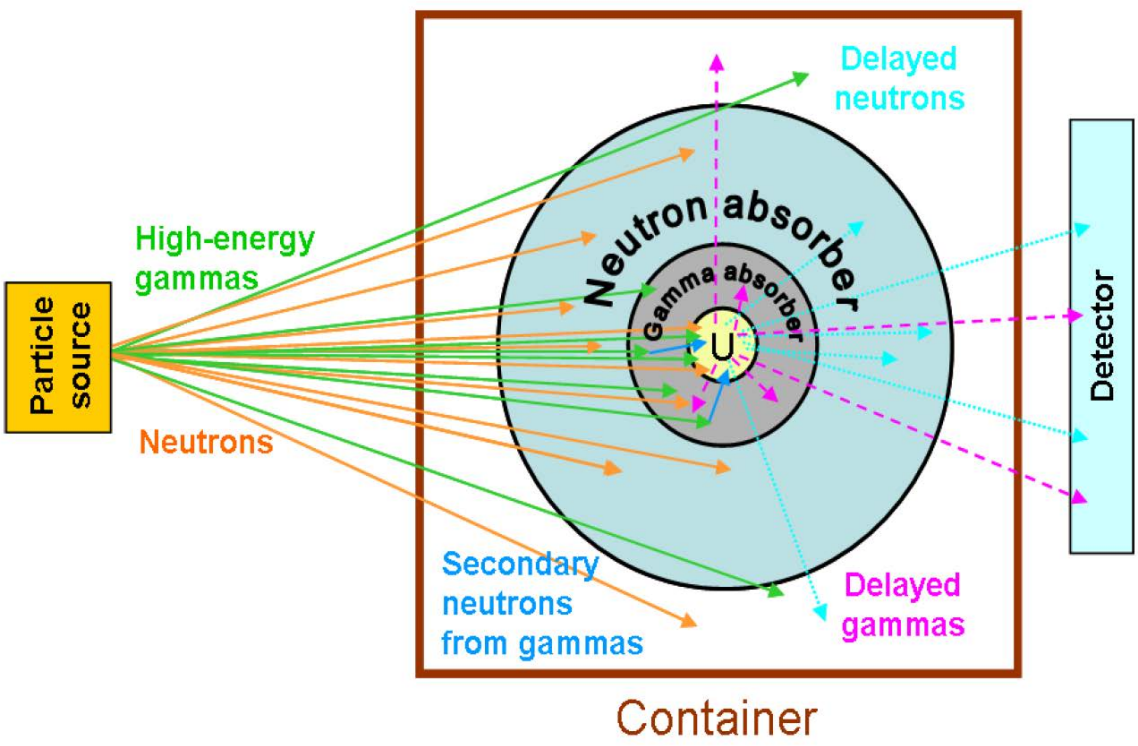

Fig. 20. Active Interrogation of Object in Container

Numerous investigations utilizing active interrogation to examine SNM detection have been performed. [22,23,24]

2.7 Background-induced Photo-fission/Neutron-induced Fission

The cosmic-ray high energy protons and helium nuclei which induce neutron and photon background have the potential to induce an additional signal from the object. This additional signal is attributed to two mechanisms: 1) the neutron-induced fission in the object; 2) the photon-induced photo-fission or spallation reactions that subsequently break apart the nucleus in the object. Photo-fission occurs when the photon energy exceeds the energy of the Giant Dipole Resonance (GDR), typically ~6 MeV, in the high Z elements, i.e., Z greater than 50. Unlike the intrinsic source, these sources are not explicitly included in the source definition in MCNP on the SDEF card. Instead these sources are implicitly included in the transport modeling of the source when the background source, described in Section 2.8, is included in the source definition. One additional MCNP specification is however needed to include the photo-fission namely the option on the PHYS card ispn≠1.

To estimate the magnitude of the photo-nuclear neutron production we have utilized a background photon source specified using the SDEF card:

sdef par=-bp loc=-30 90 0 rad=1001 sur=3 nrm=-1 wgt=155657

This SDEF setting specifies a surface source of radius 1001 cm normally directed inward. The weight was specified to match the photo-flux in the background file at the specified location, outer boundary of the object on the loc card.

The geometry of the object was a sphere of HEU (90% U-235 and 10% U-238) with a radius of 5.9819 cm with a Tungsten reflector of outer radius 16.149 cm.

The physics model card MPHYS was utilized and the PHYS:P and PHYS:N cards were specified as:

PHYS:N 3000

PHYS:P 3000 0 1 -1 0

The problem was run with the MODE n p setting and the delayed neutrons and photons were included using the act card as follows:

act dg=mg dn=model nonfiss=n p fission=n p

Using the background source, the photo-fission production was calculated to be 0.015. The total neutron leakage from the edge of the reflector was calculated to be approximately 0.017.

Note: To obtain the fission contribution from the high energy induced fissions we utilize the f8 tally in conjunction with the ft8 res 25 65 card.

NOTE: In the example above, the elevation was taken to be 0 feet above sea level. Evaluation has an effect on the magnitude of the photon flux, i.e., as much as a factor of approximately 2 at an elevation of approximately 1 km. However, given the very small photo-fission production the overall effect as discussed below is negligible.

For comparison, we performed a calculation using a background neutron source. The weight was adjusted to match the neutron flux on the outer surface of the object with the weight card and the specification of the background neutron source was made by specifying PAR=-bn. The result of this calculation indicated that a total of approximately 46 fissions occurred and approximately 113 neutrons were produced. The neutron leakage from the edge of the object was determined to be 117. Based on this calculation we conclude that the induced photo-fissions are negligible.

Finally, a calculation was performed using a spontaneous fission source distributed within the SNM. The results indicate that approximately 9.77 fission/SF occur with approximately 25 neutrons/SF. Using a spontaneous fission rate of ~$1x10^{-4}$ and 0.0064 γ/(sec g) for U-235 and U-238, respectively, we find approximately 12SF/sec. Therefore, we see that the spontaneous fission source is approximately 2.5 as strong as the background-induced neutron source.

It should be noted that in our examination of the background we have utilized a deterministically determined background that is specified in the BACKGROUND.dat file.

2.8 Background Source

Background radiation has many sources: 1) cosmic rays that pass through the magnetosphere and interact in the upper atmosphere creating particles that match the particles trying to be detected; 2) terrestrial decaying nuclides in the ground, water, or surrounding structures that emit particles trying to be detected; and 3) other sources that are not the SNM of interest.[25] As previously discussed the presence of the background neutron and photon flux impinging on an object may also create additional signal, relative to the intrinsic source, from the object which in some cases may represent a non-negligible fraction of the total signal reaching the detector. In addition, the background signal creates signal that must be differentiated from the actual signal in order to establish an actual signal from background, also known as a false alarm. (Additional discussion on this topic of detection is provided in Section 5.)

MCNP6 allows for the specification of the background source of neutrons only (bn), photons only (bp), or neutrons and photons (bg). If the user specifies bn, bp, or bg for the PAR keyword, the background spectra will be normalized to the correct magnitude for a given location using the LOC keyword. If the negative sign is omitted, the SDEF WGT keyword, i.e., source normalization is multiplied by values contained in the BACKGROUND.dat file. If the negative sign is included then the source normalization is taken only from the SDEF keyword WGT keyword.[26]

Although we have previously used the background source as a surface source, the background source is intended to be used as a uniformly distributed source within a volume. For most applications, this volume will either be a cylinder, cube, or sphere. If you start a uniform particle flux in a volume, the flux must be renormalized in order to get a flux of 1 particle/cm^2 at the geometric center of the volume. Therefore in order to get the proper magnitude of the background flux (product of 1 and magnitude of source in background file) at the center of a particular volume, the user must adjust the magnitude of the background source.[27] (It should be noted that the background source is composed of two constituent parts, the cosmic and the terrestrial source which arises from the ground and nearby structures. This source is best modeled by a surface source.)

The renormalization is related to the leakage of the geometry and therefore related to the surface area of the geometry. Several tests were completed, simulating a spatially uniform source within a void for various geometrical sizes of cubes, cylinders, and spheres, to determine adequate normalization constants, in order to set the WGT keyword. The results were as follows: 1) for a cube, wgt = SA/~3.7 (ranged 3.65-3.73); 2) for a cylinder, wgt = SA/~3.4 (ranged 3.37-3.47); and 3) for a sphere, wgt = SA/~3.0 (ranged 2.93-3.0).[28]

In many problems we are interested in specifying the background sources, i.e., neutron and photon along with intrinsic sources. In the next section we will construct several examples that illustrate how to accomplish this source construction. The intent of these examples is to illustrate

the capability of modeling the background. Fluctuations in the background from the values contained in the BACKGROUND.dat file may be as large as a factor of four or more just within the confines of a single port or port of entry. This variation arises from the widely varying distribution of NORM in the ground and structures. Consequently, when evaluating the actual ability to differentiate the signal emanating from a source relative to the background parametric evaluations must be made to account for the background fluctuations. Additional discussions on the effect of the fluctuations of the background are provided in Section 6.0.

3.0 Transport Modeling to Determine Leakage from Object

In Section 2 we presented a description of the methodology for calculating the sources relevant to the subsequent transport modeling to determine the leakage of neutrons and photons from the object. In this section we provide details of the MCNP modeling of the transport of the source to the object periphery to determine the leakages for subsequent transport to the detector. We begin by examining the relative importance of electron transport in determining the photon leakage by examining an approximate Thick Target Bremsstrahlung model in lieu of a full electron transport model in Section 3.1. Next, in Section 3.2 we examine the relative importance of including delayed particles in determining the neutron and photon leakages. In Section 3.3 we present the relative importance of the constituent source terms that contribute to the neutron and photon leakages for two different objects. The general prescription to describe multiple sources is presented in Section 3.4. Finally, two examples in which combined sources are utilized to predict the total neutron and photon leakages are presented in Section 3.5.

3.1 Electron Transport Treatment

In this section we discuss the use of the Thick Target Bremsstrahlung (TTB) model to approximate the electromagnetic radiation produced by the deceleration of a charged particle, electron, when deflected by the electrons of an atomic nucleus. This approximation assumes that the Born approximation is valid for the scattering of a photon by a free charged particle, usually an electron. This model also assumes electrons ejected from atoms are slowed to rest at the point of creation, and any bremsstrahlung radiation is subsequently transported from that point. This is a valid approximation for low energy electrons as their range in matter is negligible. For example, using the continuous slowing down approximation, the range of a few select electron energies is summarized in Table 4.

Table 4. Electron Ranges in Water and Lead[29]

Energy	Range in Water [cm]	Range in Lead [cm]
100 keV	0.014	0.0027
1 MeV	0.44	0.0070
10 MeV	5.0	0.54
100 MeV	33	1.7

For high-Z materials such as lead, the electron range is negligible for most energies. For low-Z or hydrogenous materials, the range becomes appreciable beyond a few MeV. Thus, with passive

detection in which the maximum photon energy is less than 4 MeV, using the thick-target bremsstrahlung model is a good approximation for systems that have thick reflectors. However, with active interrogation where photons and electrons with energies greater than 10 MeV may be produced, this may not be acceptable. This approximation is utilized to eliminate the computationally expensive full electron transport.

As an example of the applicability of using the TTB model, we consider our bare HEU configuration in which the source is considered to arise from the decay of the material composition specified in Table 2. Utilizing the PAR=SP source option, we present a comparison of the surface photon current for the TTB and full electron transport models in Fig. 21. (It should be noted that the intent of this calculation was to only illustrate the negligible effect of the inclusion of the time-consuming full electron transport versus a TTB model.)

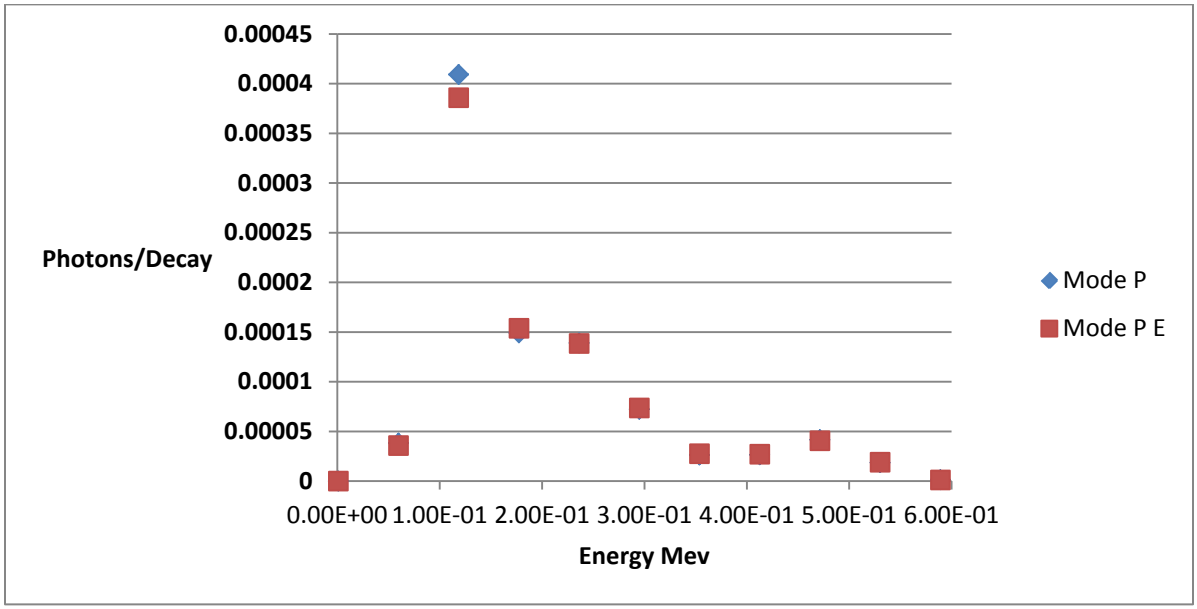

Fig. 21. Surface Photon Current/decay versus Energy

Examination of Fig. 21 reveals that the TTB model is in excellent agreement with the full electron transport calculations. This result is expected due to the fact that examination of Fig. 7 reveals that almost all of the decay photons have energies at or below 186 keV and in this energy regime the range of the electron is negligible. (It should be noted that the results presented in Figure 21 were performed with a very course spectral resolution. The intent of the calculation was to illustrate the effect of the full electron transport treatment in lieu of the TTB model. An example in which greater spectral resolution is provided is given in Section 4.)

Due to the fact that the previous example emphasized the low energy photons in lieu of the MeV photons we have examined an additional test in which the photon source consisted of a larger fraction of high-energy photons, i.e., those produced via the prompt spontaneous fission photons as well as the induced fission photons process. Figure 22 presents the results of this investigation.

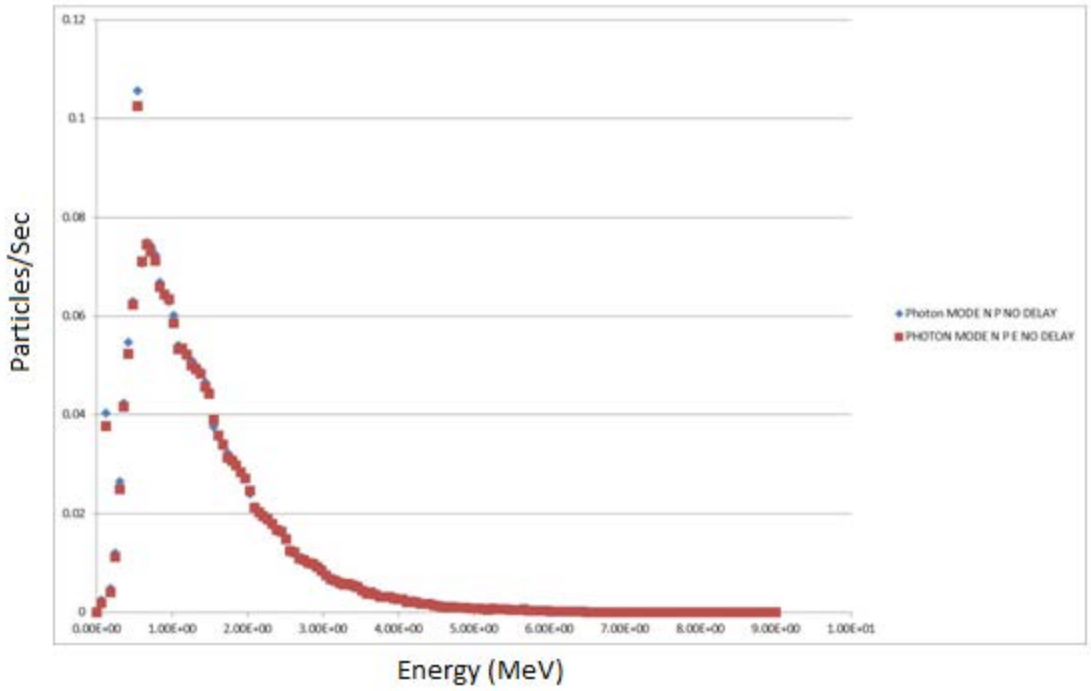

Fig. 22. Surface Photon Current/SF versus Energy SF Source

Examination of Fig. 22 also indicates that only a minimal effect is observed due to the inclusion of the full electron transport in lieu of the TTB model. Given the very negligible difference between the much more time-consuming full electron transport model and the TTB model, it is recommended that the TTB model be used for modeling the transport of photons with the object.

As expected, there was no impact on the neutron leakage using the TTB. Finally, before concluding we unequivocally state that the user should verify the appropriateness of the TTB approximation for each specific problem of interest.

3.2 Delayed Particle Examination

As we have previously discussed, both delayed neutrons and photons can be modeled with MCNP6. The delayed neutrons constitute on the order of approximately 1% of the total emitted neutrons. Furthermore, since these neutrons are all emitted within a minute and can be modeled with little additional computational cost, it is recommended that they be included in the transport simulations. Figure 23 presents a comparison of the effect of the inclusion of the delayed neutron on the surface neutron leakage energy spectra utilizing our bare HEU example.

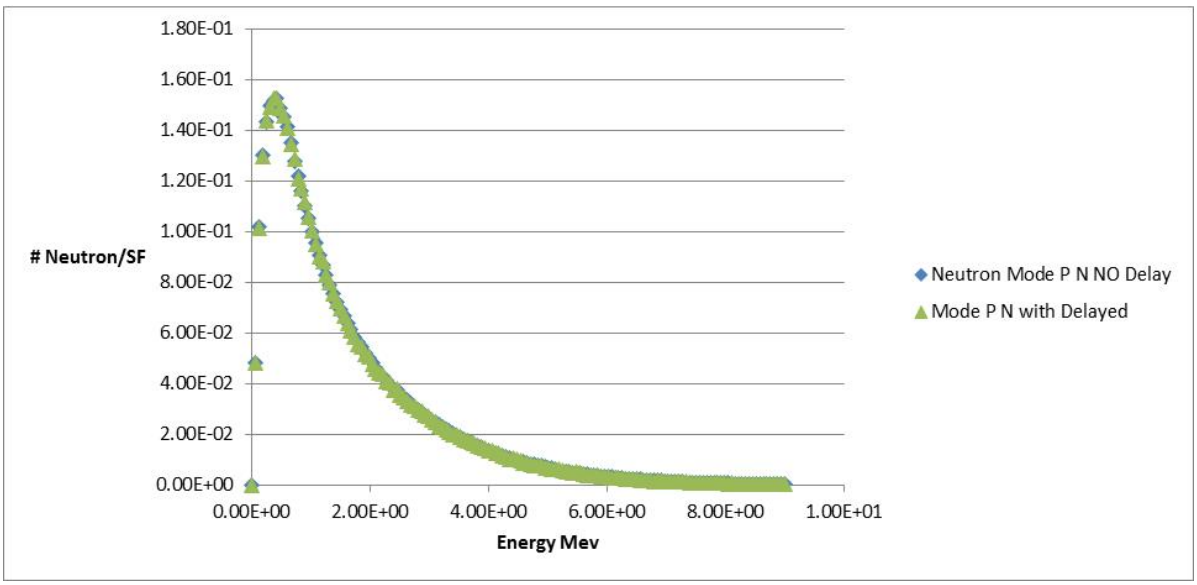

Fig. 23. Surface Neutron Leakage versus Energy w/wo Delay Particles

The effect on the photon leakage attributed to the inclusion of delayed photons may be seen in Fig. 24.

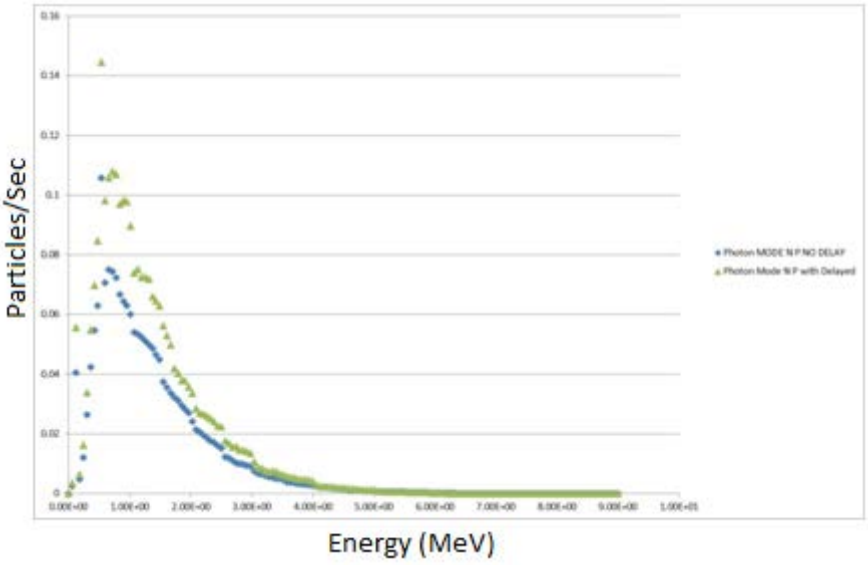

Fig. 24 Surface Photon Leakage versus Energy w/wo Delay Particles (Integrated over all time)

It should be noted that the delayed photons depicted in Fig. 24 include the time-integrated total number of delayed photons, i.e., time zero to infinity. In reality a finite count period is seconds to minutes. In Fig. 25 we present a comparison using a 5-minute count period. (However, as discussed previously, spontaneous fission events that may have occurred prior to the counting period, but within a few days have a high potential to contribute to the observed signal during the counting period.)

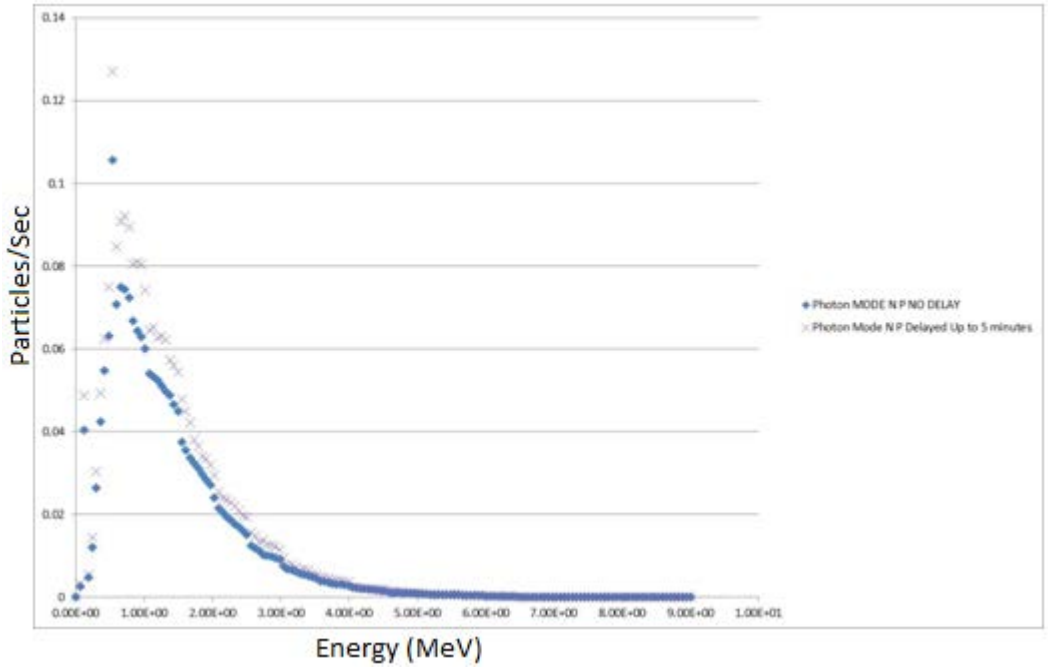

Fig. 25. Surface Photon Leakage versus Energy w/wo Delay Particles (5 minute counting)

Examination of Fig. 25 reveals that both the integrated number and spectra of the delayed photons is comparable to that of the prompt photon source. Therefore, it is recommended to include the delay photons from the spontaneous fission process. It should be noted that the magnitude of the photons generated via the fission process is significantly less than the decay source from the α,β decay. However, the energy spectra of the fission-generated photons are such that the leakage attributed to the fission photon source can exceed the decay photon source leakage in thickly reflected high Z systems.[30] Finally, we remark that due to the time-consuming nature of including the delayed photons from induced fission, it may be preferable to approximate the delayed photons from induced fission by scaling the prompt photon source by approximately a factor of 2. Additional investigations are ongoing to investigate this potentially attractive time-saving approximation. (It is again noted that a very course spectral binning was utilized in the calculation, therefore line structure was not revealed in the calculation.)

3.3 Examination of Relative Source Strength in HEU Systems

Before presenting neutron and photon leakage calculations utilizing combined sources, we first examine the relative source strengths of constituent sources for two systems. First we use the system depicted in Fig. 2 and in the second system we add a 4-inch reflector of Tungsten. These two systems illustrate important effects that need to be considered when developing combined source models to determine the neutron and photon leakages from objects.

For each of these two cases the effects of the following sources were examined: Spontaneous Fission, Spontaneous Photon, Background Neutron, and Background Photon.

The spectral neutron and photon leakages (F1 tally, current integrated over a surface) were tabulated for each of these respective systems and are presented in Tables 5 and 6 for the two respective systems. In addition the neutron/photon inward current is also presented in the tables. The inward current represents the incoming background source when either the background neutron or photon background is included. In those cases in which neither the intrinsic photon or neutron source is present the incoming flux represents the reflected source from the air that encompasses the object as may be seen from Fig. 26.

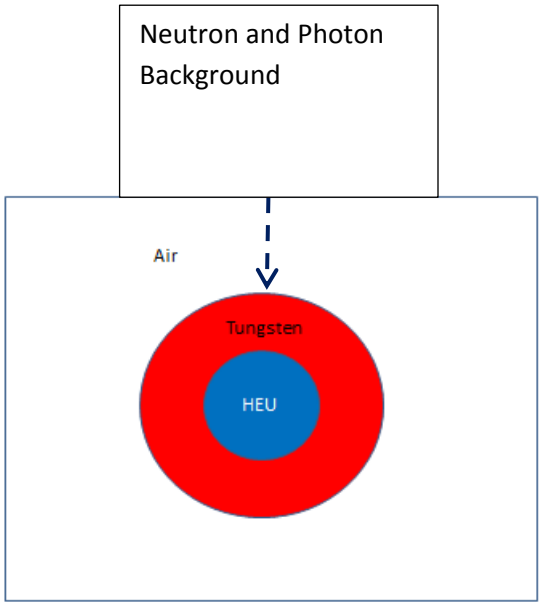

Fig. 26. Reflected HEU System with Tungsten Reflector in Air with Background Sources

Table 5. Bare HEU 17 kg Source Contributions

Source	Inward Photon Leakage /Source Particle (Cosine bin -1 to 0)	Outward Photon Leakage /Source Particle (Cosine bin 0 to 1)	Inward Photon Leakage	Outward Photon Leakage	Inward Neutron Leakage /Source Particle (Cosine bin -1 to 0)	Outward Neutron Leakage Source Particle (Cosine bin 0 to 1)	Inward Neutron Leakage	Outward Neutron Leakage
SP	9.54e-7	9.15e-4	701	6.73e6				
SF	6.3e-4	2.71	0.013	57	2.22e-3	4.49	0.04	95
Bp	1.3e-4**	1.13e-4	3710*	3225***				
Bn	6.93e-7	8.56e-5	0.067	8.44	1.33e-4**	2.25e-4	13**	21.97

* Background Photon

** Background Neutron

*** Combination of photons passing through the object in addition to scatter

Examination of Table 5 reveals that the inward directed photon current attributed to the background is 3710 photons integrated around the surface of the object. This background is much greater than either the induced photons created by the background neutron or the spontaneous neutron source. (It should be noted that the inward directed photons created by the backscatter of the photons with the air results in a slight difference in the inward/outward photon current on the boundary of the object.) Table 5 also reveals that the spontaneous photon source from the decay of the actinides, as given by the SF source in Table 5, far exceeds the background and consequently we would expect a high likelihood of the object being detected. (Additional discussion on detection is provided in Section 5.) Given our previous conclusions with respect to the negligible contribution of the photo-neutrons and also the negligible effect of using the TTB model, we conclude that the photon transport leakage may be determined by running a photon transport problem Mode P with the SP source along with the background photon source.

Table 5 reveals an inward flux of neutrons from the background neutron source that induces fission in the object, and due to the multiplicity of the system, increases the outward neutron leakage. The spontaneous fission source created by the object exceeds the background-induced fission source as may be seen in Table 5. Due to the approximately 20% contribution for the case examined, HEU 10% U-238, it would appear that in general the spontaneous fission source for uranium-based objects as well as plutonium, because of the much higher spontaneous fission rate, would exceed that of the background-induced fission source. However, due to the 20% contribution of the induced fissions from the background, it is recommended that the coupled SF and –bn problem be utilized to determine the neutron leakage. (It should be noted that the 20% factor depends strongly on the neutron BG which varies widely, and the degree of moderation around the HEU.)

In addition to the Bare HEU Configuration, a highly reflected HEU system was examined to explore the effect of a substantial reflector/shielding on the general conclusions reached for the bare system. Furthermore, the two systems examined in some sense represent the asymptotic limits with respect to radiation signatures emanating from an object. Table 6 presents the results for the Configuration depicted in Fig. 26.

Table 6. Reflected HEU 17 kg Source Contributions

Source	Inward Photon Leakage /Source Particle (Cosine bin -1 to 0)	Outward Photon Leakage /Source Particle (Cosine bin 0 to 1)	Inward Photon Leakage	Outward Photon Leakage	Inward Neutron Leakage /Source Particle (Cosine bin -1 to 0)	Outward Neutron Leakage Source Particle (Cosine bin 0 to 1)	Inward Neutron Leakage	Outward Neutron Leakage
SP	0	1.75e-9	0	1.3				
SF	1.8e-4	.778	0.003	12.97	0.0133	17.3	.22	288

Bp	1.3e-4*	1.26e-5	3710*	359.6				
Bn	6.94e-7	9.68e-5	0.067	9.45	1.33e-4**	6.89e-4	13**	67.29

* Background Photon
** Background Neutron

Table 6 indicates that the inward-directed photon leakage using the photon background source produces a background consistent with the bare case, Table 5. As previously observed in the bare case, the background photon source far exceeds either the photons induced by the background neutron source, via induced fission and inelastic collisions, or photons induced via the spontaneous fission source by more than an order of magnitude. Consequently, both may be neglected when examining the photon leakages. Comparison of the inward/outward photon current produced by the background photon source produces a behavior that is completely different than observed in the bare HEU system. Comparison of these two results indicates that for the thick reflected system there is an order of magnitude difference between the incoming and outgoing photon flux whereas in the bare system there is no such difference. We attribute this difference in the thick reflected system to the additional absorption of high energy, i.e., > ~ MeV photons that pass through the bare system. This phenomenon may act to suppress the observed radiation of an object if the measurement is made in proximity of a thickly shielded object. This effect has been observed in actual field measurements and is known as background suppression.[31]

It may also be observed that the spontaneous photon source is negligible due to the very thick, 4 inches of tungsten, in comparison to the background source. (Examination of the photon leakage associated with the spontaneous fission source in fact exceeds that of the spontaneous photon source due to decay. This effect is attributed to the large difference in the energy spectra of the photons emitted via the spontaneous fission process, i.e., MeV range relative to the much lower energy range of the decay photons.) This reduction in the intrinsic source due to the attenuation of the decay photons, principally with photon energies less than 200 keV, is attributed to the combination of the large areal mass of the reflector ρr 193 g/cm^2, the self-attenuation of the object, and the relatively large cross-sections of photons in the 50-200 keV range, dominated by the photo-electric absorption cross-section. These factors render observation of this object, with respect to photon detection, very difficult. (Additional discussion of this object in terms of detectability is provided in Section 5.)

Finally, as may be observed from examination of Table 6, the neutron signal from the background is approximately 20% of the neutron source produced by spontaneous fission. Thus, we see that background neutron flux can produce a non-negligible fraction of the neutron leakage.

3.1 Total Source Specification

Now that we have examined the relative strengths of the sources, we describe the means by which the total source may be specified on the source definition card. That is, in many situations we are confronted with a number of sources that are simultaneously present. For example, we

consider a case in which actinides are present in an object that is surrounded by a reflector. This object is also subjected to a neutron and photon background. Figure 26 presents a depiction of this system. The actinide undergoes α and β decay as well as spontaneous fission and subsequent delayed γ production from the fission products. To describe the intrinsic and background sources we place our SNM and adjoining reflector in a box to facilitate the combined. The specification of these four sources is given by the following MCNP source description:

SDEF Par=d1 x=FPAR=d2 y=FPAR=d3 z=FPAR=d4 cel=FPAR=d5 wgt=1 erg=FPAR=d6

We note that we have specified the PAR with distribution 1 which specifies all four sources

Sil1 L –sf –bn –bp p

The probabilities for each of these four sources is computed based on the source strength #/sec for each of the respective source and specified on the sp card as:

Sp1 x y z jj

For each source a distribution number is assigned as given by distribution 6.

ds6 10 20 30

Finally, for each of the respective distributions the source energy distributions are defined. For sources that have built in distributions, i.e., SF a dummy is simply specified as:

Si10 L 0

Sp10 D 1

Whereas for a distribution in which the energy distribution is needed, e.g., for the p source specified on the Si1 card, we use the following

C MeV #/sec/cc

# si31	sp21
0	0
.06	2091269800
.1	5797113
.2	7561159

Note: the use of the # symbol to input the data in columns

Examples of the computation of these values will be given in Section 3.2.

To specify the sampling of each of the respective sources the locations for x,y and z for each of the respective sources are given by dependent source cards ds2 S , ds3 S, and ds4 S. On each of the dependent source cards a distribution, one each for x, y, and z, from which the respective sources are to be sampled is given. Using Si and SP cards the sampling is then specified in Cartesian coordinates for each of the respective sources. Finally, samples for each of the specified sources are rejected if the cells specified for each source are not fulfilled as specified by the distribution identified on the cel card.

Finally, we cannot emphasize strongly enough that the Print card should be used to examine Table 170 to ensure that all of the sources have been adequately sampled.

3.4 Neutron Transport Example

Having discussed the total source specification and the appropriate approximations for both electron transport and delayed particle production, we now present the neutron transport modeling with MCNP. Before doing so we emphasize that MCNP6 utilizes continuous neutron cross sections and as a consequence avoids problems with the wide range of energy spectrum issues that are normally associated with the use of group cross-section sets. (Typically, the group cross-section sets are valid for a given energy spectrum due to the assumed energy-dependent flux used to collapse the cross-section sets.) To determine the total multiplication of the system we do not use the k_{eff} calculation, given by an eigenvalue calculation, as a multiple to the spontaneous fission source. This is because the k_{eff} calculation, as given by an eigenvalue calculation, is strictly only applicable when $k_{eff}=1$. Instead we perform a source-mode calculation which inherently incorporates the multiplication of the system without the necessity of the assumptions with respect to the neutron flux profile that are implicitly assumed in the k_{eff} eigenvalue calculation.

As we have demonstrated in Section 2.7, the photo-neutron production is negligible in comparison to the spontaneous fission and the background-induced fission source. Consequently, to model the transport of neutrons within the object we may determine the neutron leakage from the object by using the MODE N transport option. Using the intrinsic neutron source, i.e., the prompt spontaneous fission source in conjunction with the background neutron source, we have calculated the total neutron leakage from the HEU tamped object, Fig. 26, which has undergone 15 years of aging as discussed above.

To prescribe these sources we take a box surrounding our object with dimensions 2000, 2000, 2000 cm. We include both the spontaneous neutron source and the background neutron source as part of the distribution of sources on the PAR=d1 specification on the SDEF card. The relative strength of these sources is obtained via the following calculations.

For the spontaneous fission source we evaluate the activity of the SNM and multiply this value by the branching ratio, i.e., 7.2e-11. (It should be noted that the spontaneous fission rate for U-

235 given by this value is significantly lower than the spontaneous fission rate reported in Ensslin[32] of $3x10^{-4}$/1.87.)

For the background neutron source we take the reported value at a location of `37.7 -122.7 0.196` indicated in the background file and adjust the source by a factor 0.23 to account for a variation of elevation difference relative to the values defined by the location 38 -123 which is at an altitude of 1.9 km and find 9.77e4 n/sec. That is, the specified elevation at location at 37.7 -122.7 is significantly different than the elevation in the MCNP lookup table.[33]

The complete source specification for this problem is provided in Table 7 below. (It should be noted that we have zeroed out the sp source for this problem by specifying the probability of the sp decay to be zero on the sp card. The basis for this assumption is based on the previous result in which it was demonstrated that less than one particle in 10^9 reached the outer surface of the reflector.

Table 7. MCNP Spontaneous Fission and Background Neutron Source Input

```
c ----> SOURCE
c
sdefpar=d1 x=FPAR=d2 y=FPAR=d3 z=FPAR=d4
      cel=FPAR=d5
      wgt=1         $ required for ROC.  will use sampling probability
      loc=37.7 -122.7 0.196 $ SNLL 37.7 N 122.7 W 196m
c
 si1 L   -sf   -bn    -bp  $ use -sf, -bn, and -bp to preserve weight
c NOTE -> see below for norm calculation
c        sf/total      bn/total      bp/total
sp1   0.000223  0.99977  0.0  $ 17 kg 90% 2000cm cube
ds2 S    20           21            22         $ x for sphere and
domain
ds3 S    30           31            32         $ y for sphere and
domain
ds4 S    40           41            42         $ z for sphere and
domain
ds5 L  1010         1020          1020         $ cell of godiva and
air
c
si20     - 5.9819     5.9819$ radius of godiva
sp20  0           1
si21     -1000.0      1000.0   $ x of domain
sp21  0           1
si22     -1000.0      1000.0   $ x of domain
sp22  0           1
c
si30     - 5.9819     5.9819$ radius of godiva
sp30  0           1
si31     -1000.0      1000.0   $ y of domain
sp31  0           1
si32     -1000.0      1000.0   $ y of domain
```

```
sp32  0            1
c
si40     -5.9819      5.9819$ radius of godiva
sp40  0            1
si41     -1000.0      1000.0   $ z of domain
sp41  0            1
si42     -1000.0      1000.0   $ z of domain
sp42  0
```

Note: The maximum energy cutoff for neutrons was set to 3000 to accommodate the high-energy neutrons from the background.

The results of this simulation are given in Table 8.

Table 8. Reflected HEU 17 kg Source Contributions

Source	Inward Photon Leakage /Source Particle (Cosine bin -1 to 0)	Outward Photon Leakage /Source Particle (Cosine bin 0 to 1)	Inward Neutron Leakage /Source Particle (Cosine bin -1 to 0)	Outward Neutron Leakage Source Particle (Cosine bin 0 to 1)
SF/Bp/ Bn	1.3e-4	1.3e-5	4.619e-7	1.54e-5

To compare these values with those calculated in Table 4 we multiply the numbers in Table 7 by the total #/Source Particles, i.e., the sum of the SF+Bp+Bn particles. Comparison of the results obtained from Table 7 with those obtained from the individual computations presented in Table 6 indicates excellent agreement between the two calculations.

3.5 Photon Transport Example

As we have previously discussed photons are created by the intrinsic decay of the actinides as well as the accompanying prompt and delayed gammas following spontaneous fission. In addition, the background photon source presents yet another source that needs to be incorporated into the overall source for the calculation of the photon leakage from the object. Furthermore, the interaction of neutrons from either the intrinsic neutron source, i.e., spontaneous fission as well as the interaction of the neutrons in inelastic collisions as well as the n,γ reactions, create additional sources of photons. These later two additions of photons are implicitly created by MCNP when the coupled neutron-photon transport option is invoked via the MODE card via the specification of MODE N P.

To incorporate the spontaneous photon source produced due to α,β decay we include the relative likelihood of the spontaneous photons in the source definition.

4.0 Results

In this section we present results of transport simulations of objects to determine the neutron and photon leakages. A very coarse energy group binning was utilized due to the assumption that a low energy resolution detector would be utilized i.e. PVT. We first consider five different SNM objects:

- U-233 contaminated initially with 10 ppm U-232
- U-233 contaminated initially with 100 ppm U-232
- U-233 contaminated initially with 1000 ppm U-232
- HEU – Highly Enriched Uranium
- WGPu – Weapons Grade Plutonium

The isotopic compositions of each of these respective cases are presented in Table 9.

Table 9. Initial WGPu and HEU Isotopic Composition and the Composition of U-233 Contaminated Initially with 10 ppm U-232 and Cooled for 10 Years

Reference Material Descriptor	Density (g/cm^3)	Composition (%)				
HEU (93%)	18.95	^{234}U	^{235}U	^{238}U		
		0.82	93.50	5.68		
^{233}U (initially 10 ppm ^{232}U and cooled 10 years)	18.95	^{208}Tl	^{209}Tl	^{208}Pb	^{209}Pb	^{212}Pb
		$2.37(10)^{-11}$	$4.82(10)^{-14}$	$6.07(10)^{-5}$	$2.01(10)^{-10}$	$1.40(10)^{-8}$
		^{209}Bi	^{212}Bi	^{213}Bi	^{212}Po	^{213}Po
		$1.83(10)^{-6}$	$1.32(10)^{-9}$	$4.72(10)^{-11}$	$7.00(10)^{-20}$	$7.08(10)^{-20}$
		^{216}Po	^{217}At	^{220}Rn	^{221}Fr	^{224}Ra
		$5.57(10)^{-14}$	$5.67(10)^{-16}$	$2.10(10)^{-11}$	$5.15(10)^{-12}$	$1.22(10)^{-7}$
		^{225}Ra	^{225}Ac	^{228}Th	^{229}Th	^{232}U
		$2.33(10)^{-8}$	$1.57(10)^{-8}$	$2.37(10)^{-5}$	$4.29(10)^{-3}$	$9.08(10)^{-4}$
		^{233}U				
		99.9947				
WGPu	19.84	^{238}Pu	^{239}Pu	^{240}Pu	^{241}Pu	^{242}Pu
		0.010	94.026	5.814	0.130	0.020

For each of these five different SNM objects we examine the material after four different cooling periods. The cooling periods are as follows:

- 0.1 years
- 10 years
- 20 years
- 40 years

Two reflector materials were considered: beryllium and tungsten. The following thicknesses of beryllium were used:

- 0.5 cm

- 1 cm
- 2 cm
- 3 cm

For tungsten thickness of 1, 2, and 3 cm were examined. Finally, five different polyethylene thicknesses were examined. These are as follows:

- 0
- 20
- 30
- 40
- 50

Using ORIGEN the respective isotopic compositions were determined for each cooling period. We used the Brookhaven National Lab (BNL) database to determine the gamma intensities for each of the constituents. These photon intensities were then used as the source from which the photons were sampled and transported through each of the respective objects with MCNP6. (It should be noted that all calculations were performed in the P mode using a TTB model using a weight window to facilitate the sampling of the gamma emission lines. Finally, $3x10^9$ particle histories were utilized to facilitate the energy resolution of the f1 tally to obtain high fidelity results.) Before presenting the results we first illustrate the adequacy of the source sampling and also demonstrate that sufficient particle histories were utilized by presenting Figures 27-28.

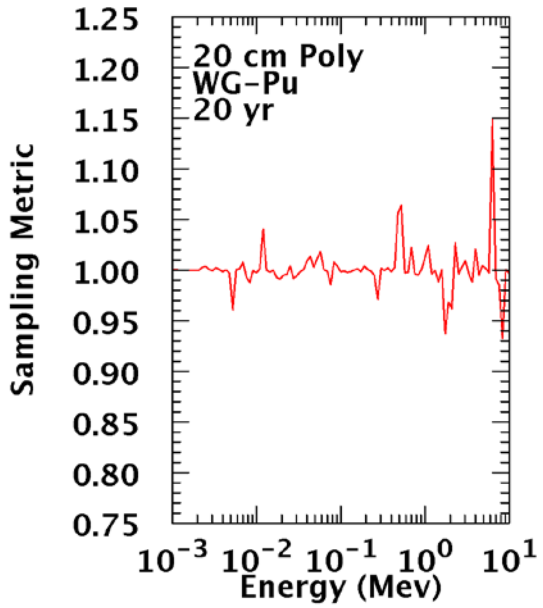

Fig. 27. Sampling Metric versus Energy

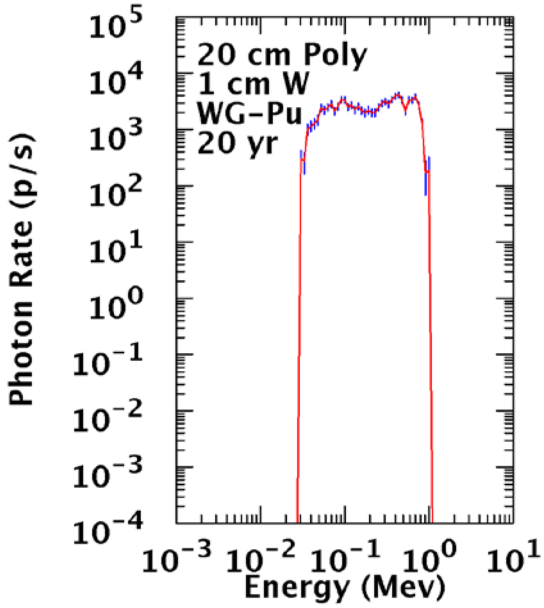

Fig. 28. Photon Rate versus Energy (Blue Error-Bars)

Note: The gamma lines are generated from the α,β decay of the actinides only.

Figure 27 demonstrates that the lines from the photon emission from uranium and its associated decay products were sampled adequately. That is, the sampling metric that compares the actual

sampling with the expected sampling is for the most part in close proximity to unity. Figure 28 presents the error bars of the F1 tally and demonstrates that adequate particle histories have been simulated, the relative error in most cases approaches 0.01. (It should be noted however that larger reflector thicknesses, i.e., 2 cm of tungsten had significant errors. However, as may be observed in Figures 29-34, the emission lines are no longer apparent due to the down-scattering of higher energy photons and consequently the energy resolution of the photon spectra is not required. Consequently, a coarse binning of the photons with respect to energy may be performed and therefore significantly improve the relative error. The results of these investigations are presented in Fig. 29-34.

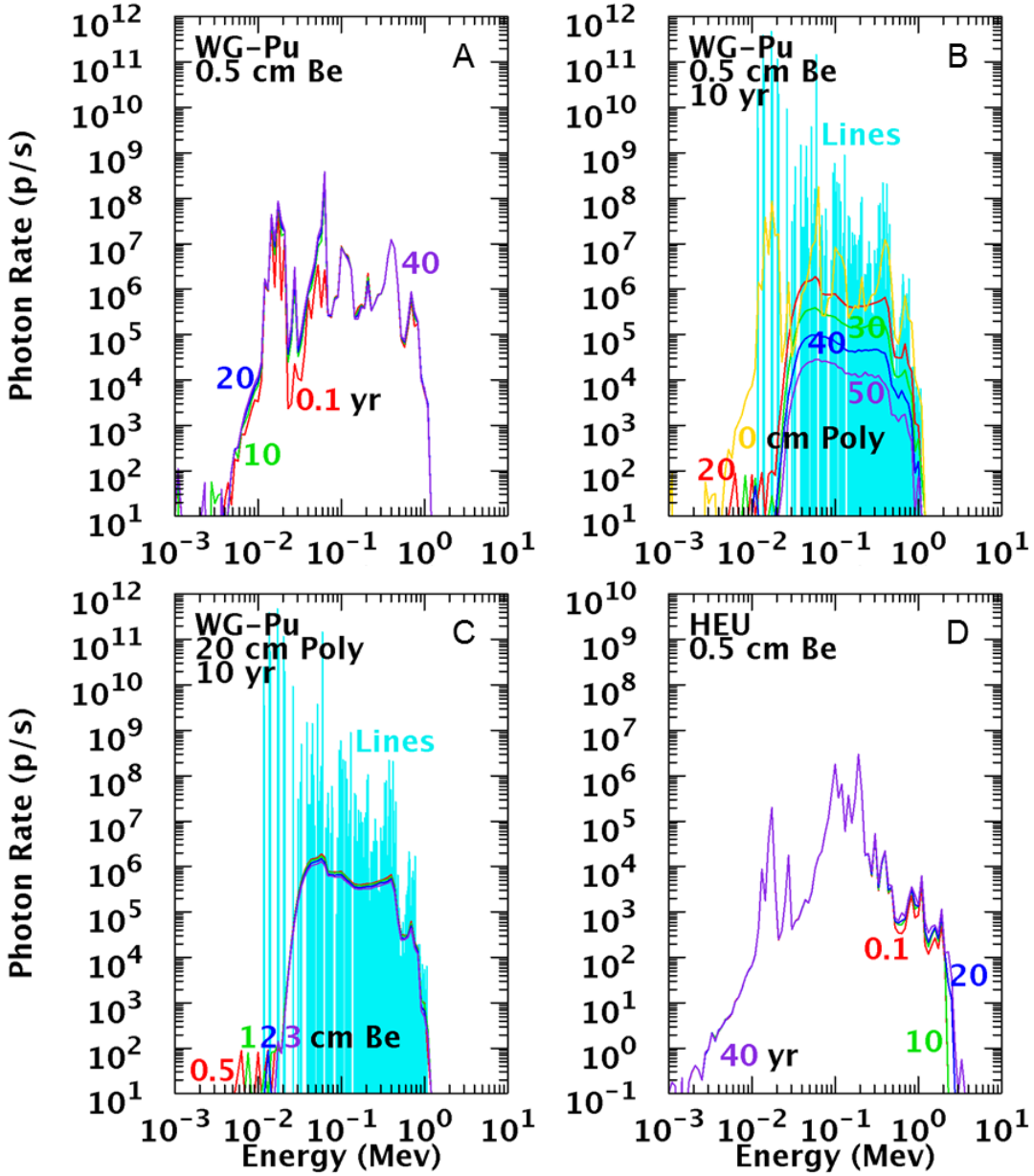

Fig. 29 A–D. Neutron/Photon Study Results

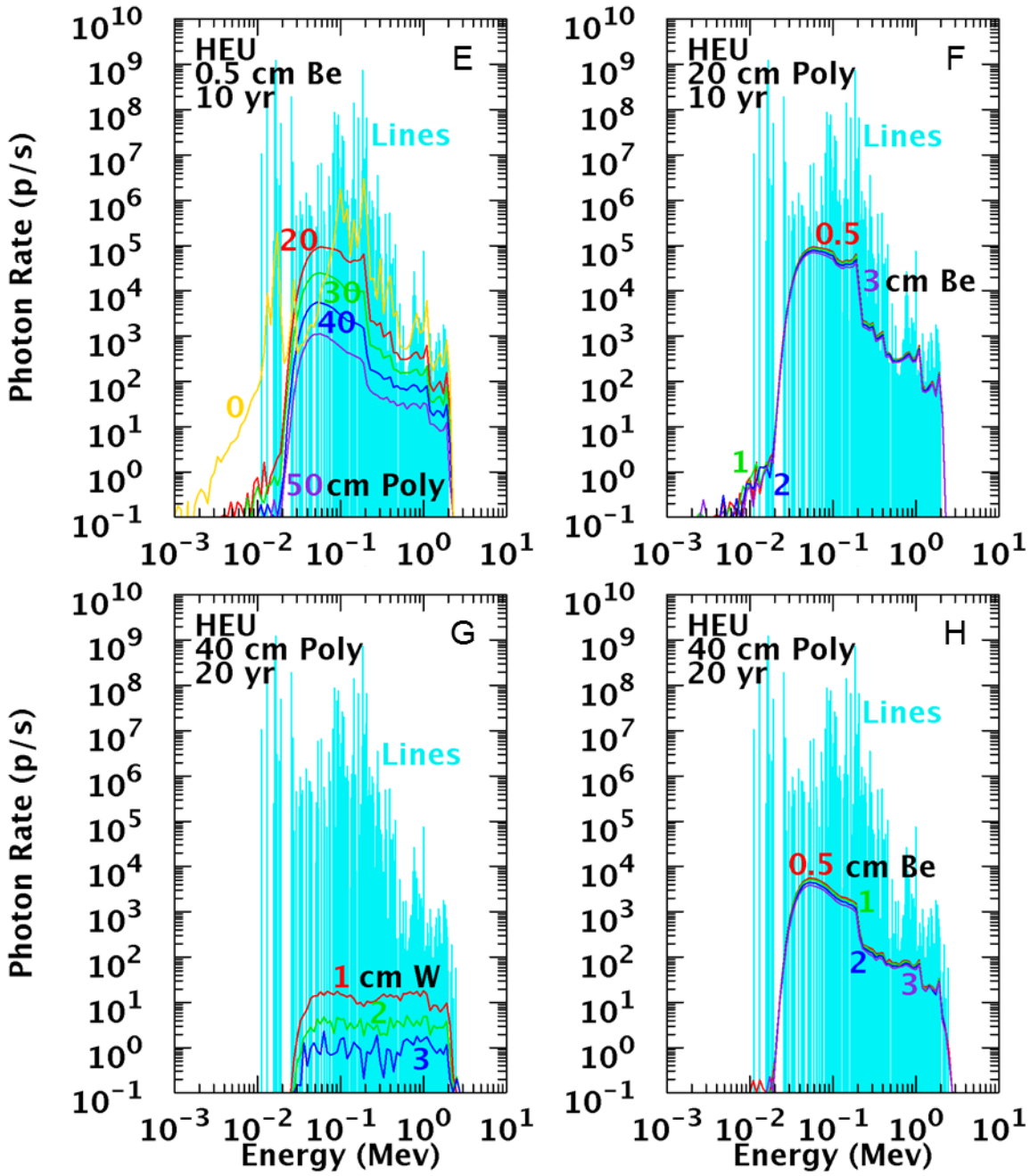

Fig. 30 E–H. Neutron/Photon Study Results

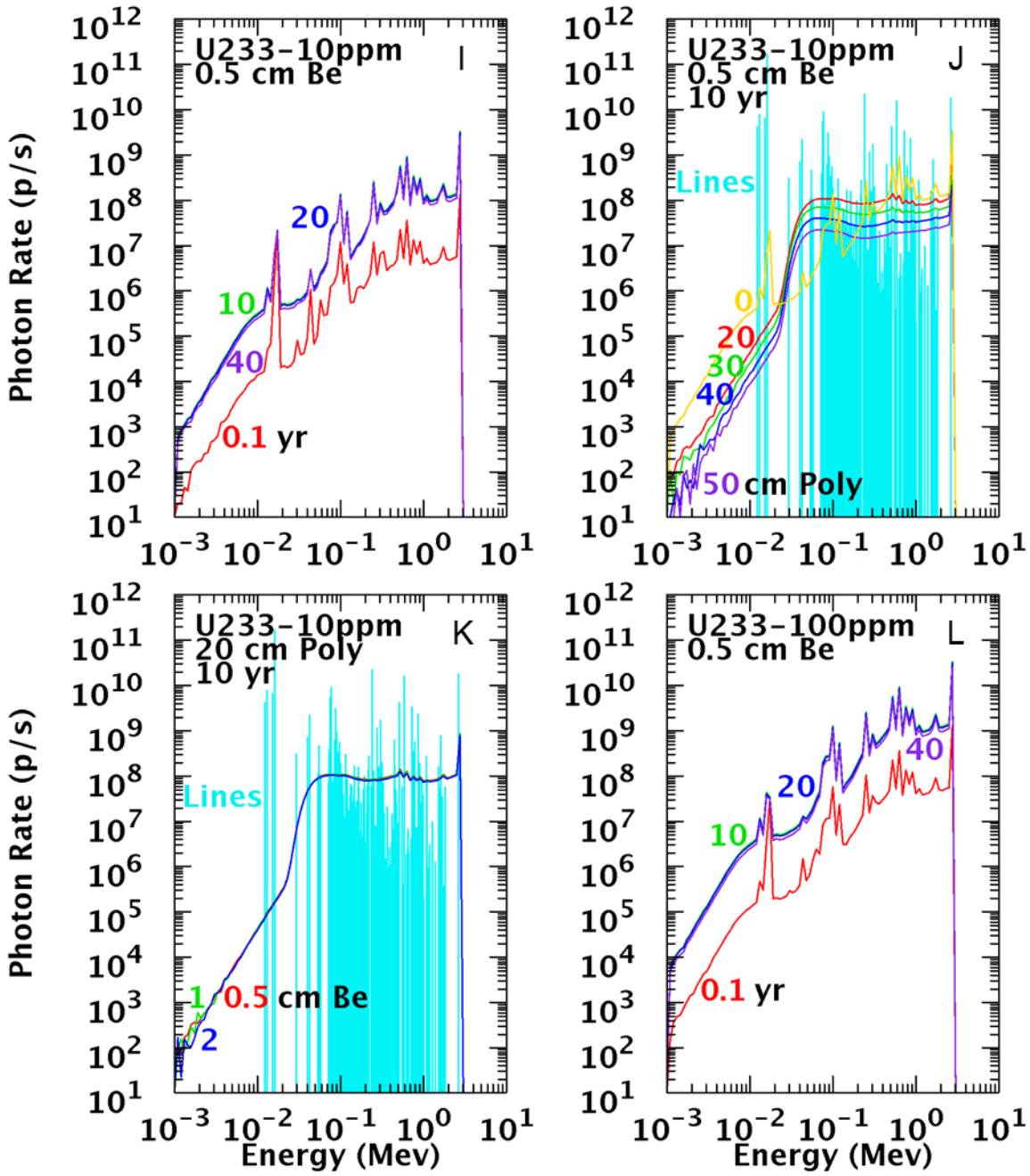

Fig. 31 I–L. Neutron/Photon Study Results

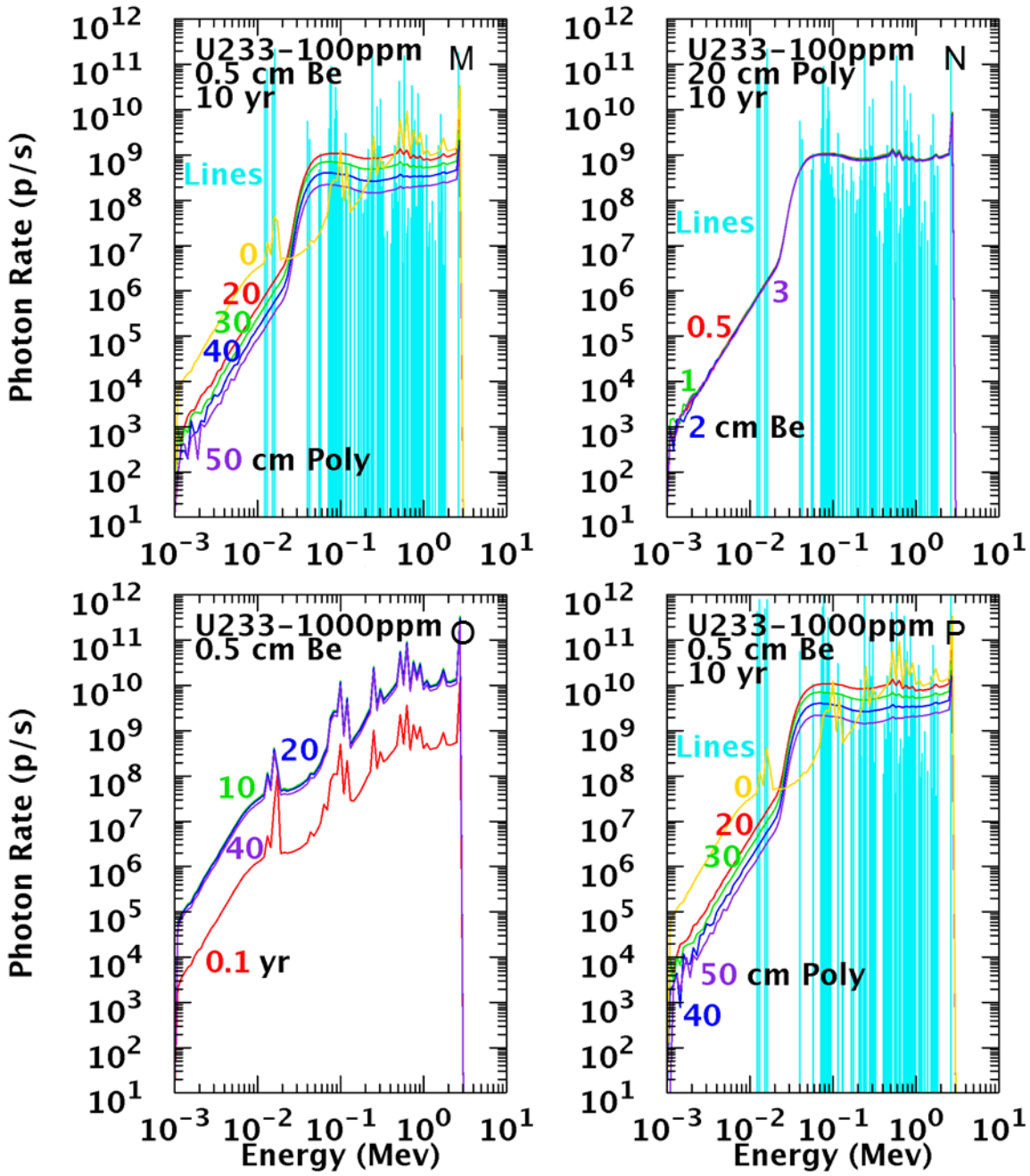

Fig. 32 M–P. Neutron/Photon Study Results

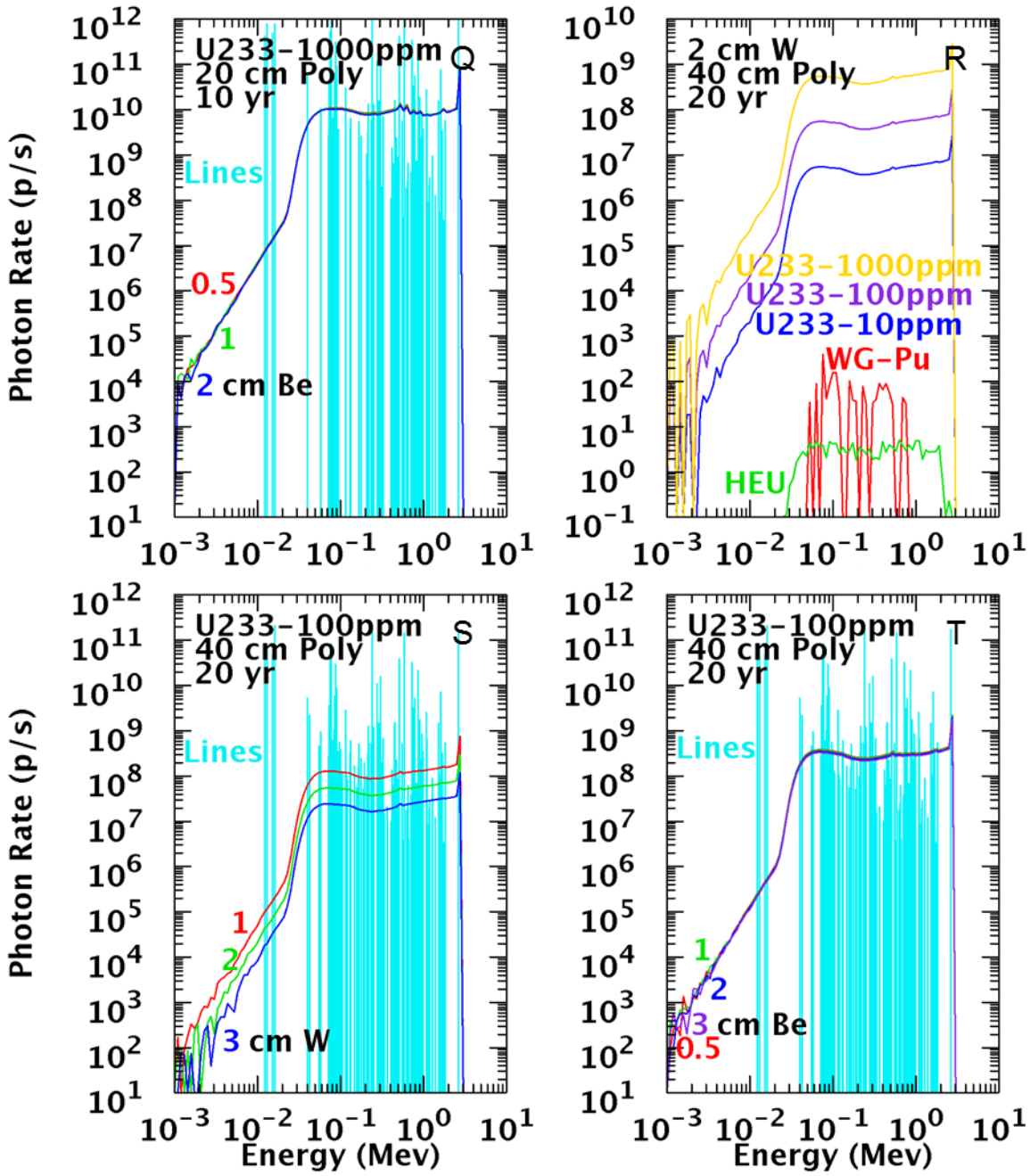

Fig. 33 Q–T. Neutron/Photon Study Results

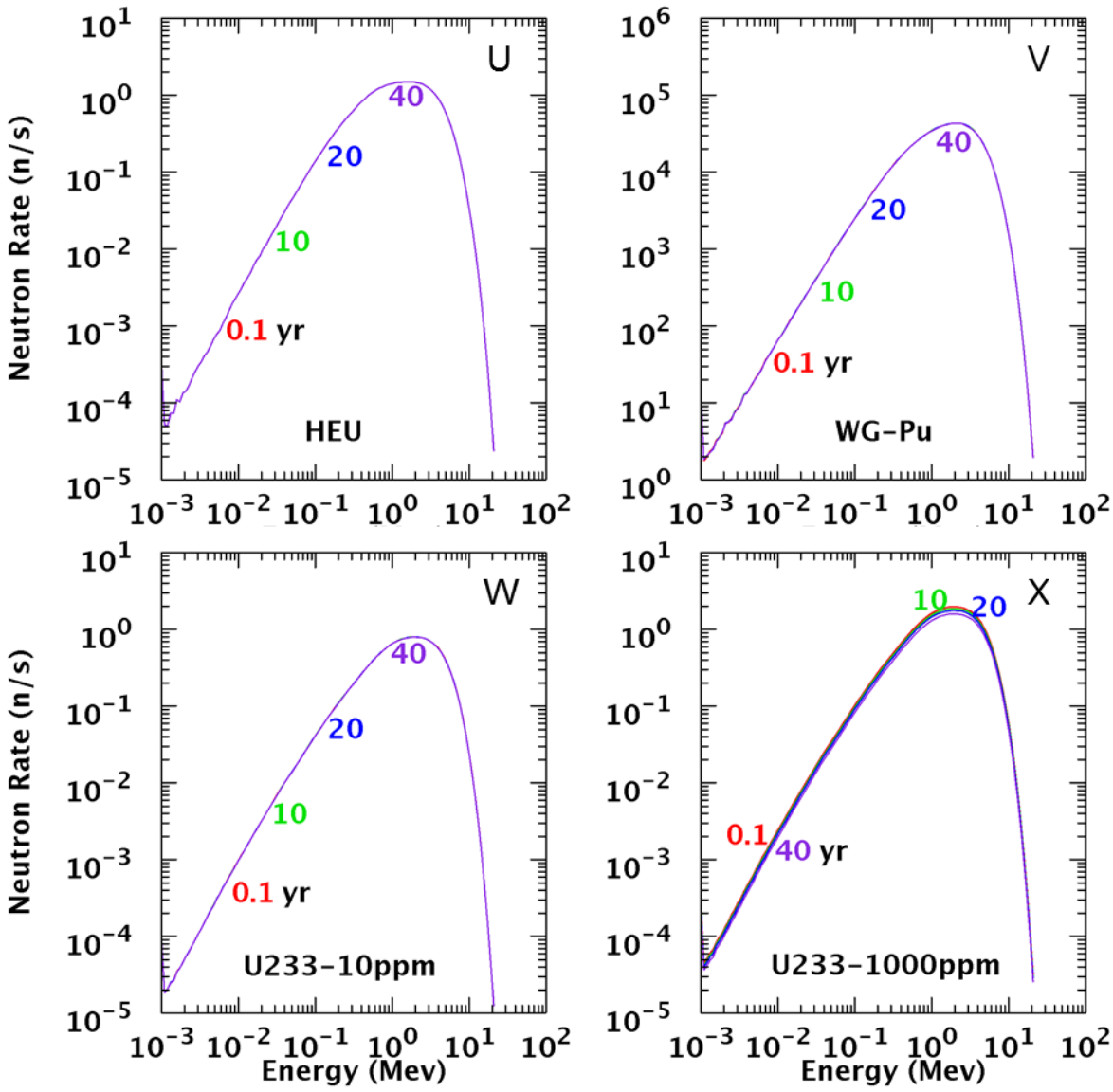

Fig. 34 U–X. Neutron/Photon Study Results

Examination of Fig. 29 A reveals that the aging of plutonium from 0.1 years to 10 years causes the activity of the plutonium to increase principally due to the buildup of americum-241 with spectral lines at 59.53 and 125.292 keV. It is also seen that after 10 years the spectral intensities are largely unchanged. Figure 29 B presents the initial lines, without any attenuating material in aqua, after 10 years of aging with a 0.5 cm beryllium reflector with varying additional thicknesses of polyethylene (HE). We notice the dramatic effect that even a relatively small amount of beryllium has on the low energy photons, reducing the sub 100 keV photon lines by approximately 3 or more orders of magnitude. Furthermore, it may also be observed that the inclusion of 0.5 cm of beryllium with no polyethylene also broadens the photon lines, via scatter, and produces a background of very low energy photons, sub 10 keV. Finally, the addition of polyethylene serves to further reduce the intensity of the photon lines and also broadens the

spectra around the lines, to the point that with 20 cm of additional polyethylene there are no discernible lines. Finally, we observe from Fig. 29 B that with each additional 10 cm of polyethylene the intensities are reduced by an order of magnitude.

The effect of increasing the thickness of beryllium, with a constant polyethylene thickness, is presented in Fig. 29 C. In this figure beryllium thickness is varied while holding constant the cooling period of the Pu and the thickness of the polyethylene. This figure reveals that for all beryllium thicknesses examined, the effect is to effectively eliminate the sub 20 keV photons with no discernible difference in the intensities above 20 keV.

Figure 29 D and Figures 30 E–H present the results of an analogous examination utilizing HEU. Examination of Fig. 29 D reveals that aging has only a very small effect on the line intensities, principally above 1 MeV due to Pa-234m. The effect of increasing the polyethylene thickness, at constant Be thickness, and Be thickness, at constant Polyethylene thickness, is analogous to those of Pu as indicated in Figs. 30 E and F, respectively. We compared the effect of replacing the beryllium with a comparable thickness of tungsten and it is presented in Figs. 30 G and H. Examination of these figures reveal that as expected the increased areal mass of tungsten relative to Be, even at 1 cm, reduces the leakage of photons from the object to very small fractions of the initial intensities, approximately 8 orders of magnitude, across the entire spectrum.

Figures 31 I–Q presents the examination of the effects of aging and variations of polyethylene and reflector thicknesses for an object containing U-233. Three different levels of initial U-232 contamination were examined in this investigation. By comparing Figure 31 I, L, and Figure 32 O, the effect of increasing the initial U-232 contamination is to significantly alter the magnitude of the photon intensities in the 0.1 to 3 MeV spectral regions. In addition, Figures 31. J, K and Figure 32 M, N, P, and Figure 33Q the effect of the variations in the beryllium and HE thicknesses on the photon intensities in the 0.1 to 3 MeV regions is minimal.

Figure 33 R presents a comparison of the spectral intensities for the materials examined (WGPu, HEU, and U-233) with 2 cm of tungsten, and an outer layer of 40 cm polyethylene with 20 years of aging. To further examine the magnitude of the U-233 spectral intensities, we may compare this system to the other systems. As may be seen in Fig. 33 R, the U-233 systems have by far the largest intensities over the entire spectral range. Finally, a comparison of the effect of reflector material, beryllium and tungsten for the U-233 object is given in Figs.33 S–T. Unlike the other materials in which the inclusion of tungsten reflector was sufficient to effectively reduce the spectral signal for all photon energies, the initial intensities for the 100 ppm U-233 system are such that significant signal is still present above approximately 50 keV even with the addition of 3 cm of tungsten reflector.

Figure 34 U–X present the neutron intensities for each of the respective materials examined. As expected the effect of aging does not alter the neutron emission rate, as given by the spontaneous fission, and consequently the neutron emission is independent of aging.

As previously discussed the previous parametric investigations utilized a very course binning of the energy spectra. To demonstrate the ability of MCNP6 to calculate the fine line structure that may be experimentally measured we have performed a calculation of the HEU (10 yr aged) system with 0.5 cm Be with 20 cm of accompanying polyethylene. The results of this simulation are presented in Figure 35 along with an experimental measurement supplied by Mark Abhold of NEN-3.

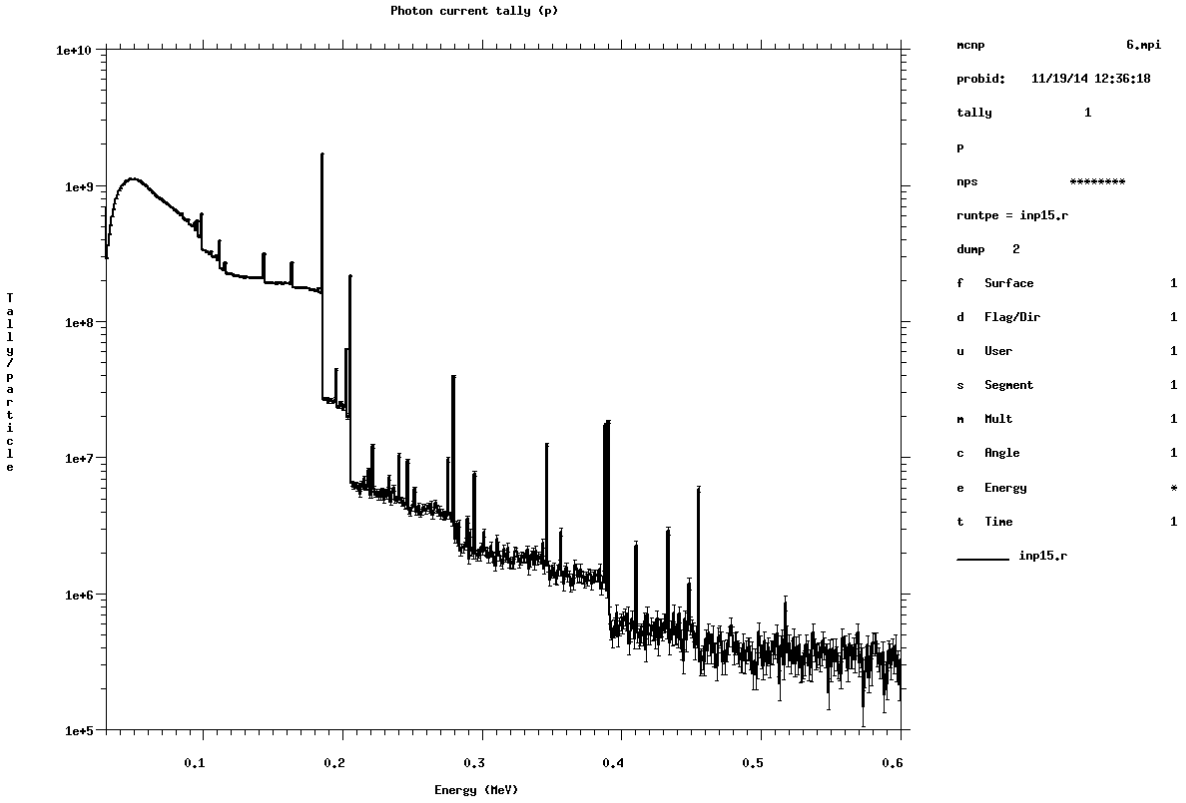

Figure 35 Counts versus Energy (HEU (10 year Aging) with 0.5 cm Be and 20 cm of Polyethylene

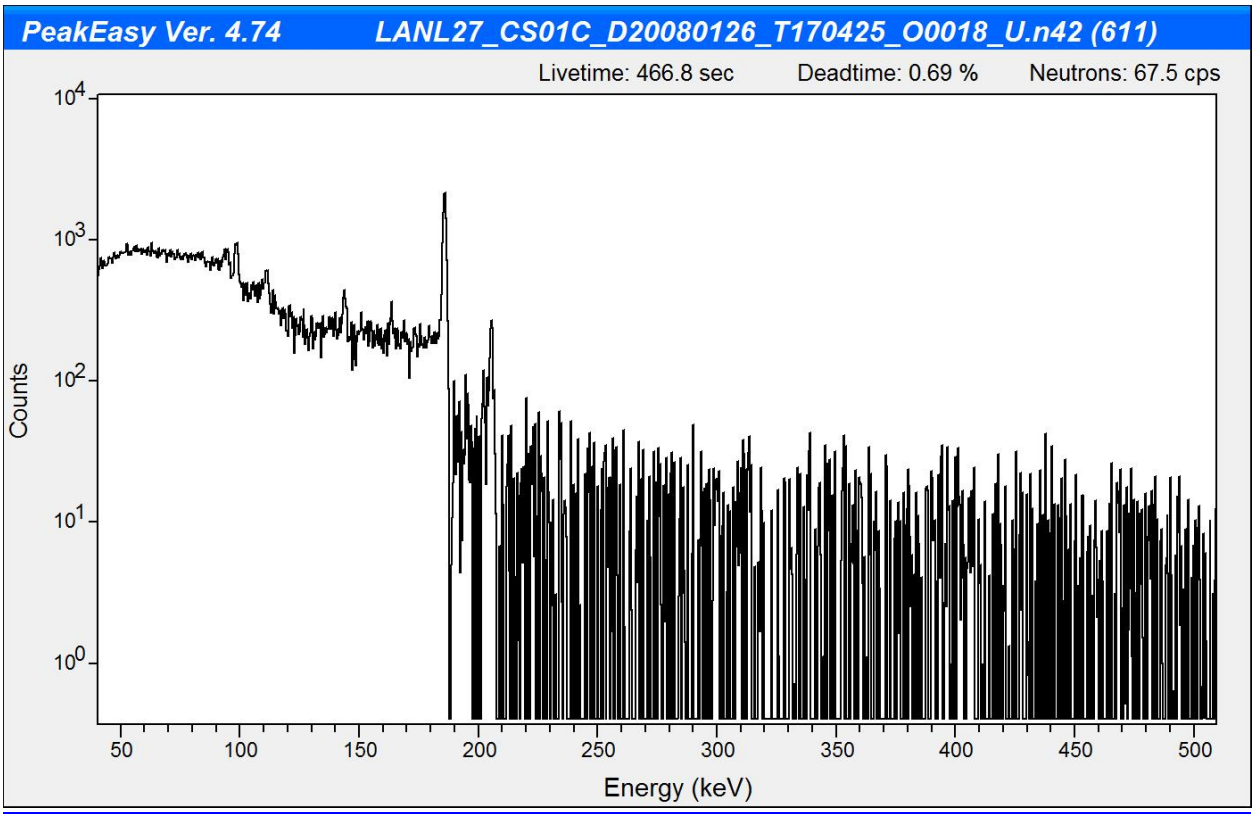

Figure 36 Experimental Measured Spectra for1 Kg HEU with 20 cm polyethylene with HPGe

5.0 Detectability of Objects

In Section 4.0 we presented details on the use of MCNP to model neutron and photon leakages from objects. In addition, numerous examples were presented to elucidate the pertinent physics to facilitate the efficient calculation of these signals from several objects. As part of this investigation we have discussed the fact that the low energy photons emanating from an object are very susceptible to absorption via any extraneous shielding that may exist between the object and the detectors. In addition, we have observed that the presence of the object can even modify the nearby background signal. Consequently, developing a means by which to evaluate the detectability of objects, i.e., metrics, needs to be carefully evaluated. For example, metrics that use low-energy photons may be very susceptible to large variations when even thin shielding is present between the object and the detector. Thus, in order to properly evaluate the detectability of an object we must now examine the actual environment in which the object resides and also the actual registration of a signal based on the neutron/photon current imparted on a detector and the detector characteristics. Consequently, in Section 5.1 we present a general discussion of the scene in which an object may exist. In Section 5.2 we present a brief discussion of detector modeling for both neutrons and photons with the MCNP tallies. Finally, in Section 5.3 we discuss the means by which to determine detectability of objects and introduce the newly developed capability within MCNP6 to calculate ROC curves that may be used to determine detectability of objects.

5.1 Scene

In the previous sections we have prescribed a methodology to calculate the neutron and photon leakages from the object. These leakages may be captured for subsequent calculations in which the neutrons and photons are transported across the scene of interest to the detector. (It must be emphasized that the total source from the object must be calculated. That is, any induced source from the background must be included in the leakages from the object.) In MCNP6 this is performed by writing the source using the SSW card and then reading this source for subsequent transport using the SSR card. Alternatively, the source may be obtained from the output from the tally and used as input for the subsequent transport calculation. An illustration of the differentiation of the object and the scene is presented in Fig. 37.

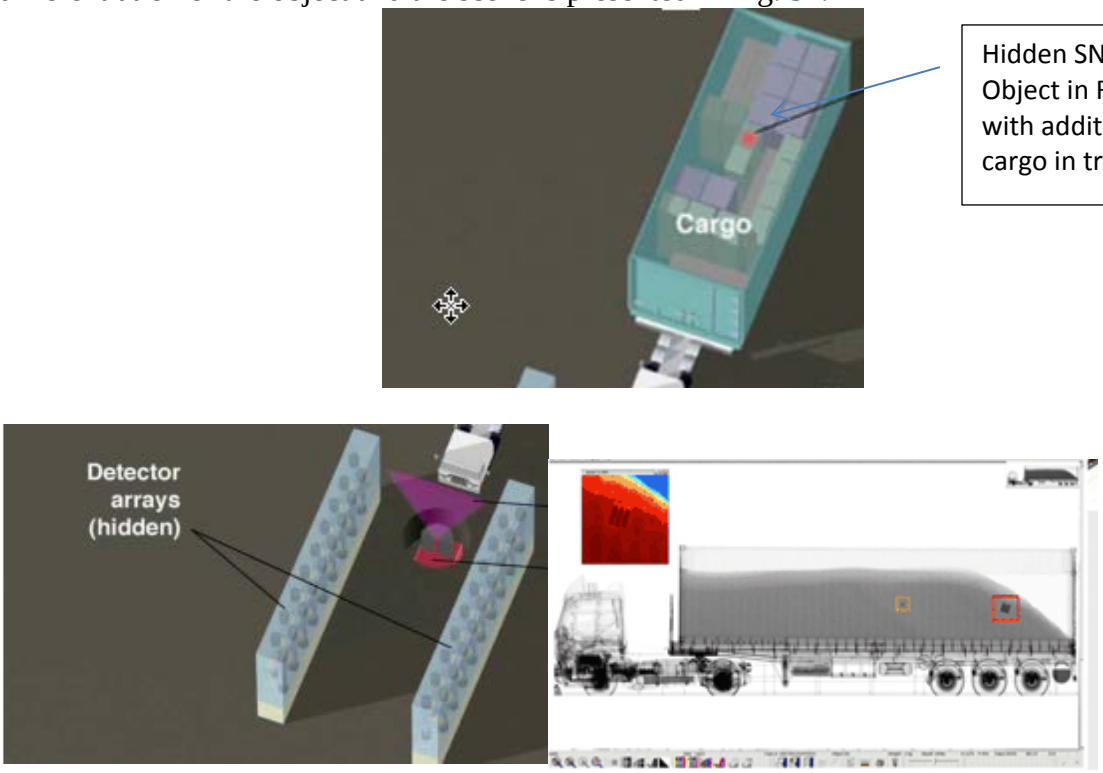

Fig. 37. Hidden SNM in Cargo Container, Detector Configuration, and Radiograph of Container[34]

In general Fig. 37 shows some degree of three-dimensionality exists in describing the scene. The level of detail included in the calculation will undoubtedly depend on the fidelity of the intended results.

It is also noted that the scene may have a significant effect on the neutron signal. In fact it has been observed that increased neutron counts are usually registered around large sources of water, such as oceans. Water is an effective moderator of neutrons. Near air/water interfaces, cosmic-ray neutrons have a higher thermal flux and lower fast flux than seen in free air.[35] Additionally, the neutron flux near an air/steel interface has been observed up to 25 times the flux at an air/water interface.[36] Around large ships, elevated neutron count rates are observed due to the production of spallation neutrons from cosmic rays striking the metal in the ship.[37] This is called the “ship effect.” Ship-effect neutron rates are dependent on latitude, altitude, weather, and solar

activity. However, personal watercrafts are too small to elicit this reaction, as this is observed around tens of tons of high-Z material.[38]

5.2 Detectors

The neutrons and photons that emanate through an object and scene ultimately arrive at a detector. Since both photons and neutrons have no electrical charge, their energy is converted to electrical pulses that can be measured. In the remainder of this section we briefly discuss the detection of photons and neutrons and then present a discussion on the use of MCNP to model the detection process.

5.2.1 Detecting Gamma Rays

Gamma rays do not have an electrical charge, and create no direct ionization or excitation of the material through which they traverse. To detect gamma rays, a conversion process in which the photons interact with the electrons in the materials. There are two main ways to turn a gamma ray into electrical energy. One is with a scintillator material, such as PVT. Scintillators are materials that, when struck by photons of higher energy, such as gamma rays, capture this energy and release it as photons of lower energy, usually visible light. (The energy states of the material, determined by the crystal lattice or in the case of PVT, the amorphous plastic, allow the scintillation process to occur.) One of the requirements of the scintillator material is that it should capture as much of the energy of each photon striking it as possible in order to build an accurate photon energy spectrum and thus identify the material emitting the photons. Ideally, a photon should deposit its full energy in the scintillator material, a so-called full-energy interaction. It is also important that the deposited energy be efficiently converted into photons of visible light, which are then counted to determine energy. There are two main types of scintillators. Inorganic scintillators (those not containing carbon) are typically single crystals, such as sodium iodide (NaI) with a small amount of thallium added and organic scintillators such as polyvinyl toluene (PVT).[39]

The probability of full-energy interaction increases sharply with atomic number (Z) of the scintillator material. The more energy from each photon a scintillator absorbs and then gives off, the better the correlation between energy input and output, and the more precise the spectrum that can be constructed. As a result, a device using an inorganic crystal has a good ability to identify the radioactive material producing a gamma-ray spectrum. There are however several drawbacks most notably the area of a detector that is sensitive to gamma rays is small (limited to the size of a crystal), so the detector must be close to the object to be searched or must scan for longer time so it can receive more gamma rays. In addition they are fragile and are sensitive to light, so they must be protected from environmental conditions.[40]

In contrast to the scintillator, a semiconductor material, such as HPGe, turns gamma rays directly into an electrical signal proportional to the gamma-ray energy deposited. A voltage is applied across the material, with one side of the material the positive electrode and the other the negative electrode. When a gamma ray interacts with the material, it knocks electrons loose from the semiconductor's crystal lattice. The voltage sweeps them to the positive electrode. Their motion produces an electric current whose voltage is proportional to the energy of each gamma ray. Each pulse of current is then sorted into a bin depending on its voltage and the spectrum is computed as described above.[41]

Detectors require a signal-to-noise ratio high enough to permit detection. That is, they must extract the true signal (such as a gamma-ray spectrum) from noise (such as spurious signals caused by background radiation). Two concepts are central to gamma-ray detector sensitivity: detection efficiency and spectral resolution. Efficiency refers to the amount of signal a detector records. Radiation intensity (e.g., number of photons per unit of area) diminishes with distance. Since a lump of SNM emits radiation in all directions, using a detector that is larger, or that is closer to the SNM, increases the fraction of radiation from the source that impinges on the detector and thereby increases efficiency. Another aspect is the fraction of the radiation striking the detector that creates a detectable signal. A more efficient detector collects data faster, reducing the time to screen a cargo container.[42]

Spectral resolution refers to the sharpness of peaks in a gamma-ray spectrum. A perfect detector would record a spectrum as vertical "needles" because each radioactive isotope releases gamma rays only at specific energies. Since detectors are not perfect, each energy peak is recorded as a bell curve. Polyvinyl toluene (PVT), a plastic used in radiation detectors that can be fielded in large sheets at low cost, is efficient but has poor resolution. It can detect radiation, but peaks from gamma rays of different energies blur together, which can make it impossible to identify an isotope. Figure 38 shows the spectra of 90% U-235 and background radiation as recorded by a PVT detector. In contrast, high-purity germanium (HPGe) produces sharp peaks, permitting clear identification of specific isotopes. These detectors are expensive, heavy, have a small detector area, and must be cooled to extremely low temperatures with liquid nitrogen or a mechanical system, making them less than ideal for use in the field. Figure 39 shows the spectrum of Pu-239 as recorded by detectors with better resolution than PVT.

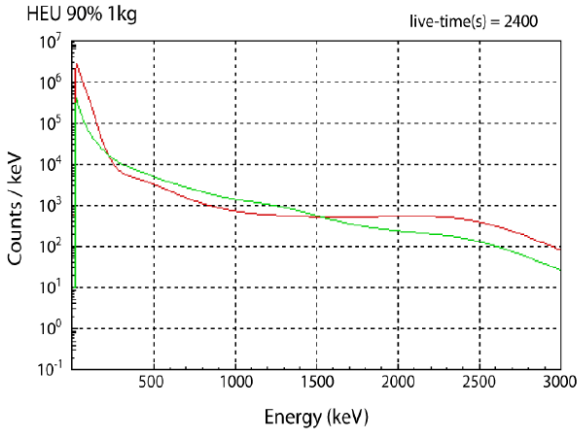

Source: Lawrence Livermore National Laboratory.

Notes: Spectra were taken with a PVT detector at a distance of 1 m and computed with GADRAS. Uranium is unshielded, background is dirt. The uranium-235 line starts as the upper line (in red) at far left.

Fig. 38. Gamma-Ray Spectra: 90% U-235 vs. Background, Taken with PVT[43]

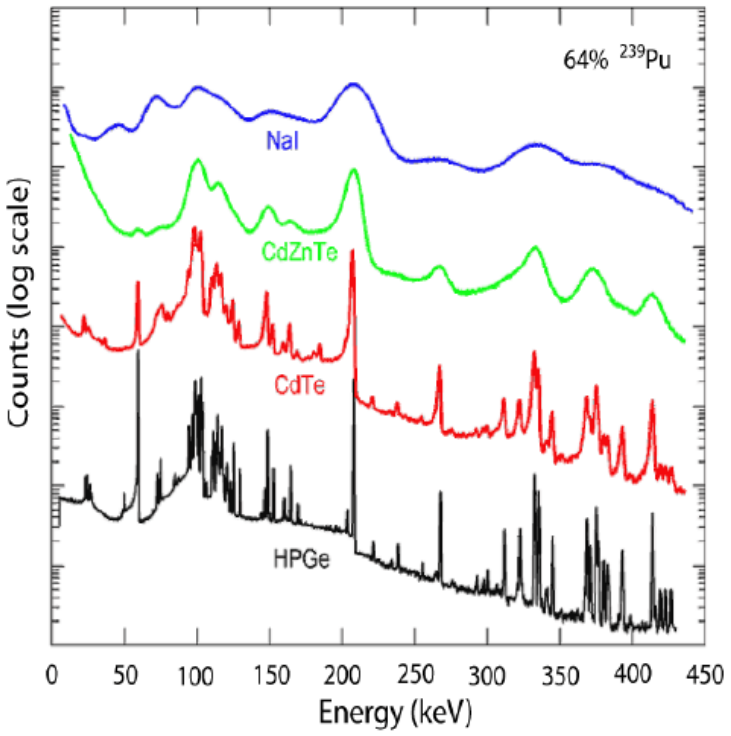

Fig. 39. Gamma-Ray Spectra Pu-239 Inorganic Scintillating Materials[44]

Figure 38 shows that plastic scintillator detectors have very poor energy resolution but even the crude energy information they offer can be used to determine if SNM is present. These systems count the number of photon interactions in the detector and signal an alarm if the count rate exceeds a threshold that is dictated by the local background count rate. This method of alarming on only the count rate relative to background is termed gross counts (GC) and is the simplest type of alarm algorithm. Typically, the total counts may be compared with background to determine if SNM is present above a statistically significant level or a passive algorithm of this type such as an energy windowing (EW) algorithm may be used.[45] The EW algorithm bins the crude spectral count rates into energy windows (large energy bins). After binning, the count rate in each of the energy windows can be compared to that of the background spectrum in the same window to determine if a threat is present. The EW data can be compared to the background spectrum in multiple ways. Typically, a ratio of the counts (or count rate) in an energy window to some other quantity (counts in a reference window, total counts over all windows, etc.) is used. These ratios are then compared to the same ratios calculated for the background spectrum and an alarm is signaled if the ratios differ by a predetermined amount defined by the background spectrum and acceptable false positive rate.[46] Additional discussion on more methods of detecting SNM are provided in Section 5.3.

5.2.2 Detecting Neutrons

Neutrons are neutral particles and do not interact in matter through the Coulomb force. Due to their lack of charge, neutrons can pass through materials without interacting, making it

impossible to directly detect them. However, neutrons can be detected by their interactions with nuclei, which produce secondary radiations, often in the form of heavy charged particles. To maximize the probability of interaction and production of secondary radiations, it is necessary to use materials with high neutron absorption cross sections. One such material is helium-3 which has absorption as the dominant interaction for neutrons below energies of 10 keV, as can be seen in Fig. 40. Around 0.025 eV, the energy of thermal neutrons, the absorption cross section is 5330 b.[47] The nuclear reaction by which neutrons interact with ^{3}He is given by:

$$n + {}^{3}He \rightarrow {}^{3}H + {}^{1}H + 0.764\ MeV \qquad \text{Equation 5}$$

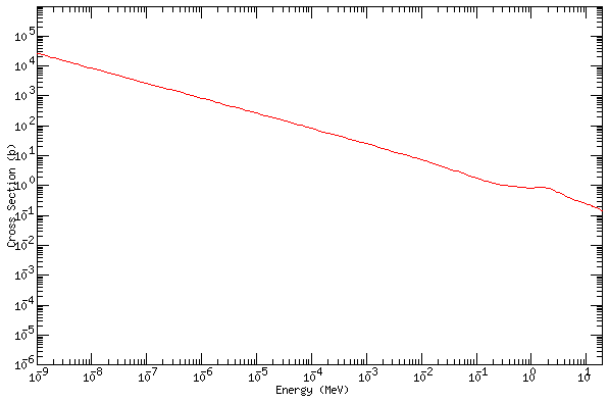

Fig. 40. Absorption Cross Section of ^{3}He[48]

A common neutron detector is a tube of ^{3}He gas linked to a power supply, with positively and negatively charged plates or wires in the tube. (Because capture reactions are highly probable at thermal energies, these tubes are usually surrounded by a hydrogenous thermalization medium such as plastic.) In its rest state, current cannot pass through the helium because it acts as an insulator. When a low-energy neutron passes through the tube, a ^{3}He atom absorbs it, producing energetic charged particles that lose their energy by knocking electrons off other ^{3}He atoms. Positively charged particles move to the negative plate; electrons move to the positive plate. Since electric current is the movement of charged particles, these particles generate a tiny electric current that is counted. Tubes are manufactured in a variety of sizes, but can be up to 7 cm in diameter and 100 cm in length. Like photon detectors, they may be placed in an array to increase the solid angle and absolute detection efficiency.[49]

Finally, it is noted that neutron detection can be advantageous because the presence of neutrons above background is a strong indicator of the presence of SNM, as most nuisance sources do not emit neutrons. In the case of weapons-grade plutonium (WGPu), the spontaneous fission source strength of ^{240}Pu makes unshielded WGPu relatively easy to detect if neutron detection is available. However, background neutrons from cosmic and terrestrial sources limit the minimum detectable activity from a neutron source and can be a source of false alarms.

5.3 MCNP Modeling of Detectors

In Section 3 we described the process to simulate the transport of neutrons and photons to the outer surface of an object. As discussed in Section 3 this source could then be used to subsequently transport through a given scene to a specified detector location. To simulate the acquisition of an inferred signal from these particles, it is necessary to model the detector. MCNP has a very well documented and benchmarked history of performing this task. In Figs. 41-43 we present some comparisons between experimental data (counting time 3600 sec) and MCNP with a sodium iodide detector (Ortec model 905-4) using simple sources.[50] Figure 41 presents a comparison of the full peak efficiency between the NaI physical detector response and MCNP. In this study a source at a distance of 15.24 cm from the detector face was simulated at energies varying from 10 keV to 2 MeV in 10 keV steps to determine the energy response of the simulated 3x3 NaI detector.[51] The same test was performed using the physical detector at several energies from the available sources. The results are shown in Fig. 41. Results indicate a good comparison between the simulated and experimental energy responses.

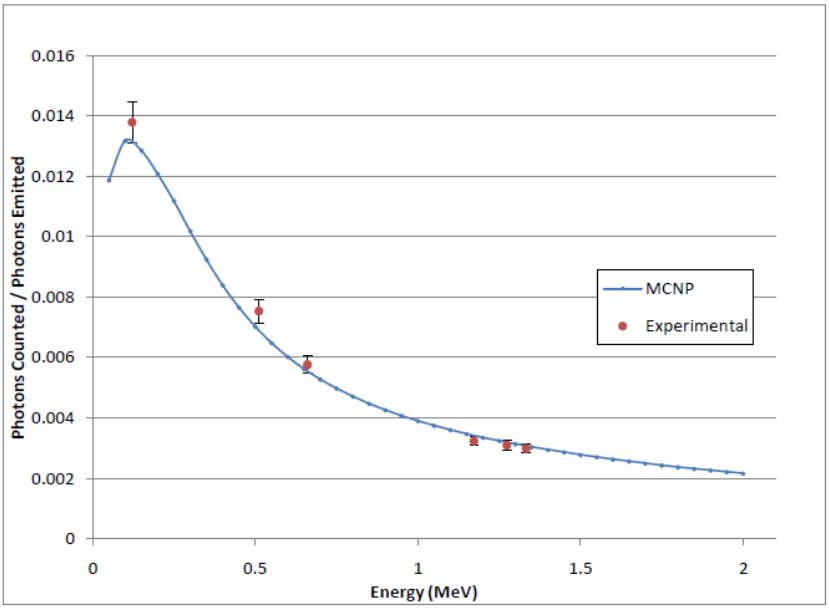

Fig. 41. Comparisons of 3X3 NaI Detector Energy Efficiency using Cs-137,Na-22 and Co-60[52]

Figures 42-43 present comparisons between MCNP simulations, using a NaI detector, and both Co-60 and Cs-137 sources.

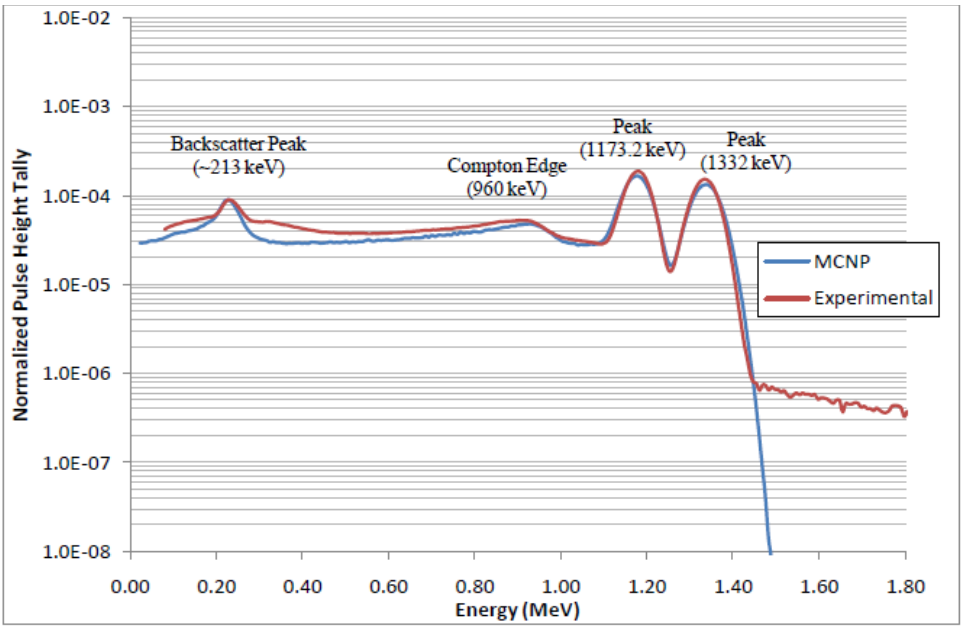

Fig. 42. Comparisons of 3X3 NaI Co-60 Full Energy Spectra[53]

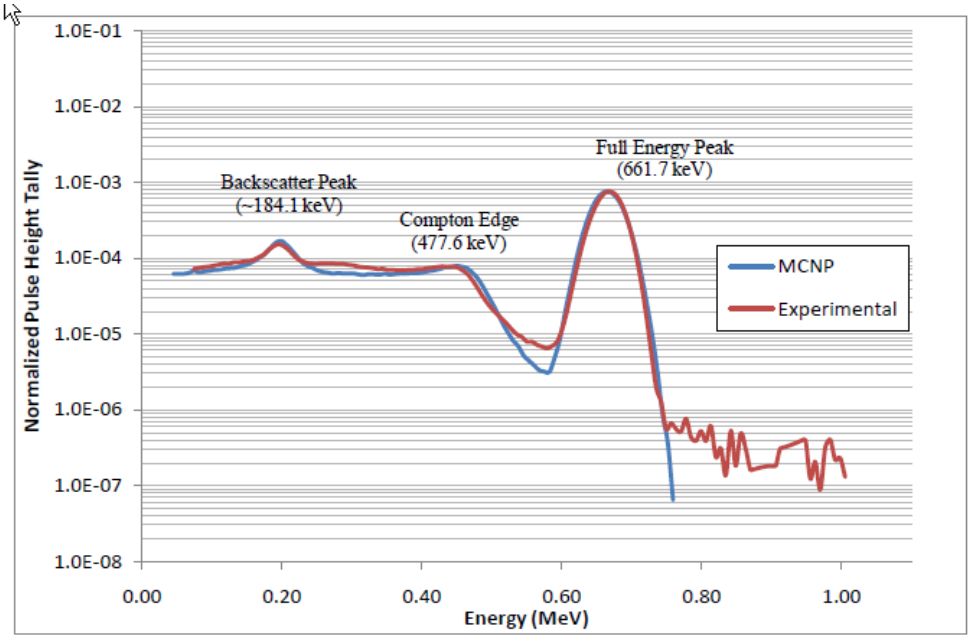

Fig. 43. Comparisons of 3X3 NaI Detector with Cs-137 Full Energy Spectra[54]

In the remainder of this section, we briefly describe the modeling process for both neutrons and photons using the MCNP tallies.

MCNP uses tallies to estimate quantities of interest to the user. For example, an f4 tally is the average cell flux tally and counts the particle track lengths, or distances traveled by each particle, through a cell volume. The units of an f4 tally are particles/cm^2. Specification of energy bins

may be applied to this tally to determine the neutron and photon spectra in the detectors. For neutron detection this is important in the design space due to the fact that the ^{3}He detectors require thermalization for efficiency and consequently calculations may be performed to determine the requisite moderation necessary.

MCNP also allows for the pulse height tally F8, and energy binning, to determine the distribution of pulses created in a cell that models a physical detector. Although the entries on the F8 card are cells, this is not a track length cell tally. F8 tallies are made at source points and at surface crossings. The pulse height tally is analogous to a physical detector. The F8 energy bins correspond to the total energy deposited in a detector in the specified channels by each physical particle.

In order to convert an f8 tally into count rate (s^{-1}), it must be multiplied by the activity of a source. To account for energy broadening due to the energy resolution of the detector, MCNP allows for Gaussian energy broadening of the pulse height tally to assist in mimicking the resolution of a physical detector. This is accomplished by defining the full width at half maximum (*FWHM* in MeV) using the expression[55]:

$$FWHM = a + b\sqrt{E + cE^2} \qquad \text{Equation 6}$$

Where: *E* is the energy of the particle in MeV and the parameters *a* (in MeV), *b* (in $MeV^{1/2}$) and *c* (in 1/MeV) are supplied by the user.

MCNP models for a ^{3}He SNAP neutron detector and a NaI detector are presented in Appendix A.[56,57]

6.0 Detectability

In the previous sections we have described formalism for modeling the radiation signatures that may emanate from an object and reach a detector through a prescribed scene. As previously discussed the signal from the object of interest that reaches the detector may also be accompanied by signal that is a direct consequence of the background which is composed of both cosmic and terrestrial components. Therefore, determining the detectability of an object requires differentiation of the signal produced via the object and the stochastic background field. In fact, as we shall see the signal also exhibits a degree of variability with respect to the registered number of counts on the detector.

Traditionally, the differentiation between the signal and the extraneous background is determined by measuring the background field and then measuring the object in question a short time later. A comparison is then made between the observed signal and the previously measured background to determine if the object is emitting a radiation signal, which may be a threat object. (This approach implicitly assumes that the background is stationary, i.e., that it does not substantially change during the time in which the object of interest is examined and that the object does not alter the background signal.) The decision process is typically based on setting a

threshold above which a positive indication of the presence of a threat object is made. Determination of the threshold is typically based on a trade-off between obtaining a false-positive signal and a false-negative. Some illustrations of possible signals from sources in conjunction with background are depicted in Fig. 44.[58]

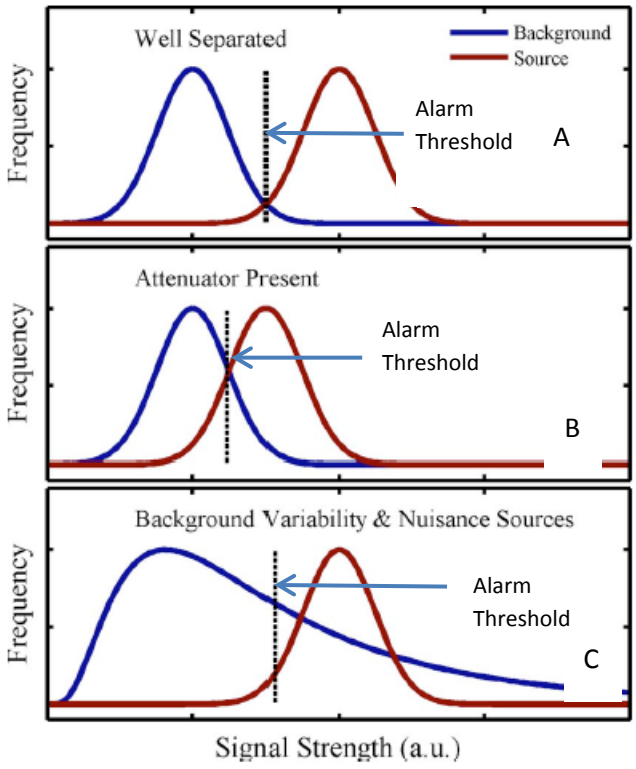

Fig. 44 A-C. Alarm Settings for Source and Background Configurations[59]

As may be observed from examination of Fig. 44, in those cases in which the signal and the background are well separated, the area under the blue curve to the right of the dotted line is small. This area represents the probability of a false alarm, i.e., false positive. The probability that an alarm is signaled when there is no actual signal, other than background, is possible. Minimization of false alarms is an objective. Conversely, to the right of the alarm threshold depicted in red represents the probability of detection, i.e., true positive. This is the probability of detecting an actual object that emanates a signal in the presence of a background signal. Two additional probabilities complete the four possible detection outcomes. These are the probability of a false negative. This is the probability that an object emanating radiation is actually present but the alarm threshold is such that the alarm does not trigger. This is effectively a miss in the detection of an actual threat object and is to be minimized. Finally, there is the probability of a true negative signal. In this case no radiation source is present above background and no alarm

trigger is actuated. (We note that the probability of the true negative and false positive distributions and the true positive and false negative should both sum to unity.)

The desire to minimize the probability of false alarm while maximizing the probability of detection necessitates that a decision on the alarm threshold be made. Before addressing the selection of the alarm threshold we return to Fig. 44. Examination of Fig. 44 A reveals that when the two distributions are well separated, an alarm threshold may be selected so as to minimize the false alarm probability while allowing for a high probability of detection. The addition of an attenuator that serves to largely affect the signal emanating from the object effectively brings the two curves together and hence may lead to either a significant probability of false alarm or reduce the probability of detection if a low false alarm probability is desired.[60] Finally, distortion of the background as depicted in Fig. 44 C not only to issues associated with a decision that must be made with respect to acceptance of high false alarm or reduction in the probability of detection but also introduces an additional complication in that the background probability distribution is not a simple Poisson distribution. This tail to the background distribution may significantly affect the false positive probability. This additional complication will be discussed in more detail in the next section.

6.1 ROC Curve Background

The desire to minimize the probability of false alarms while maximizing the probability of detection necessitates a decision with respect to the level at which to set the alarm threshold. For a given technology, these objectives cannot be achieved simultaneously—an improvement in either one comes only at the expense of the other. A receiver operator characteristic (ROC) curve, such as Figure 45, provides insight into this relationship.[61] By relating the true positive and false positive rates, the curve defines the performance of a receiver (in signal processing, where the term "ROC" originated) or of nuclear detection equipment. ROC curves show that the probability of a true positive and a false positive go up together. This tradeoff is shown in Fig. 38 by moving from point C, with a high probability of detection but a high false alarm rate, to point B, with intermediate values for both, to point A, with a low false alarm rate but a low probability of detection.[62]

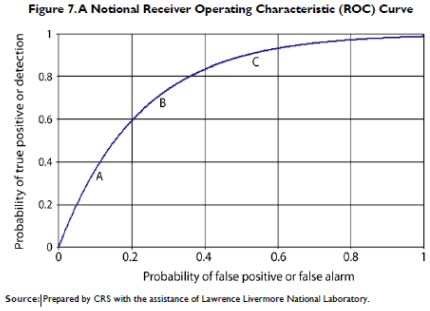

Fig. 45 Hypothetical Receiver Operating Curve[63]

To illustrate a few concepts we present Fig. 46 which shows three ROC curves to illustrate several concepts: (1) Moving from curve A to curve B to curve C shows the performance of several hypothetical detectors.[64] The improvement can be visualized by moving upward (line 1), which shows an increase in the true positive rate for a given false positive rate, or by moving from right to left (line 2), which shows a reduction in the false positive rate for a given true

positive rate. (A diagonal line from lower right to upper left would show improvement in both.) (2) A, B, and C could represent differences in performance of one detector under different conditions, such as changes in the background, different operating conditions (e.g., scan time), or different benign materials in a container. ROC curves are thus highly useful in comparing alternative detection technologies and also investigating alternatives with respect to detector settings needed to achieve policy objectives and operational constraints simultaneously, where the probability of false alarm translates directly to operational costs.[65]

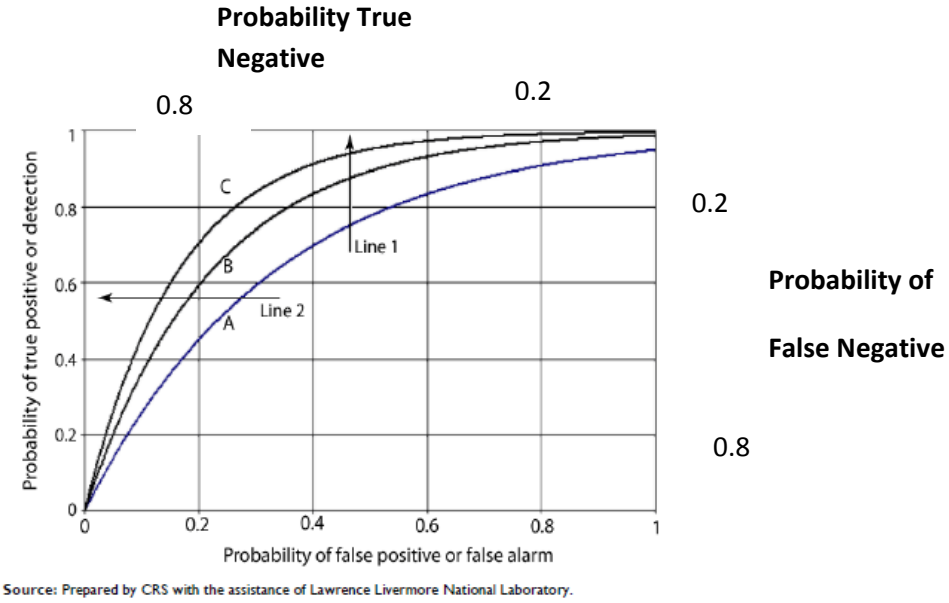

Fig. 46. Illustration of Trade-Offs in Probability of Detection and Probability of False Alarm

Finally, we note that many variables may affect the receiver operating curve including:

- Detectors
- Detector Count Time
- Source/Detector Relative Distance
- Environmental Conditions
- Shielding between source and detector
- Background Strength/Variability
- Source Strength and Spectral Content as given by a spanning set of threat objects

In the next section we describe the use of MCNP to generate ROC.

6.2 Generation of ROC Curves with MCNP

In this section we outline the procedure by which MCNP may be used to generate ROC curves. This procedure is based on simulating the actual number of source particles that are emitted from all sources during a specified counting period repeatedly and performing this process repeatedly to generate the probability distributions for both the signal and the background. From these two distributions the cumulative probability distributions or ROC may be generated. It should be

noted that this procedure is needed in those cases in which the underlying distributions cannot be assumed to be Poisson processes. Otherwise a single calculation may be used and the assumption with respect to the Poisson distribution may be used to generate the ROC. It should be noted that unless the transport model incorporates correlated events then a Poisson distribution is expected due to:

- Each history represents either a score or a non-scoring event,
- Each event is of low likelihood, and
- The number of sampled events is large.

The fission process is known to create correlated events that are not well represented by a Poisson distribution. An example of this is presented in Fig. 47.

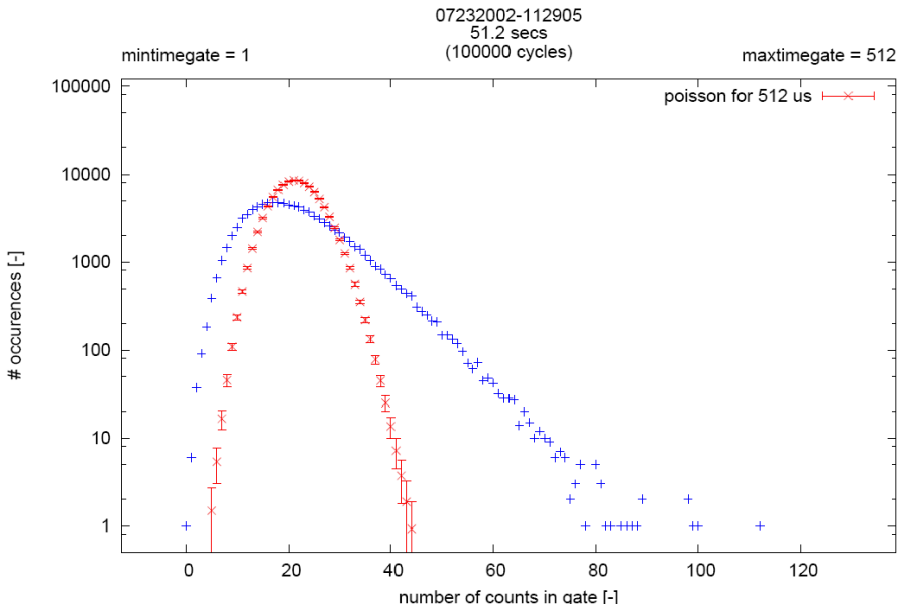

Fig. 47. 4.4-kg Pu Fission Source Moderated by 3.3-Inch-Thick Polyethylene Count Distribution 512-□-thick Time Gate, after 10^5 Observations[66]

It should be noted however that the ability to observe non-Poisson behavior is a very strong function of the ability of the detector to detect correlated counts. This ability is significantly reduced by the distance and hence solid angle that is subtended by the object. Furthermore, the MCNP tally specification must be carefully considered when attempting to capture the non-Poisson behavior. That is, tallies that aggregate quantities such as the f6 tally generally are not capable in discerning non-Poisson behavior if used to simply register a score or non-score and not discriminate based on the quantity of energy imparted by the neutrons, which would be a measure of the number of neutrons creating the detector pulses and thereby an indicator of non-Poisson behavior, i.e., numerous arrivals.

The distribution using the f6 tally in conjunction with an f8 PHL tally has recently been shown for a 1-kg HEU object to approach a Poisson.[67] Figure 48 presents these results.

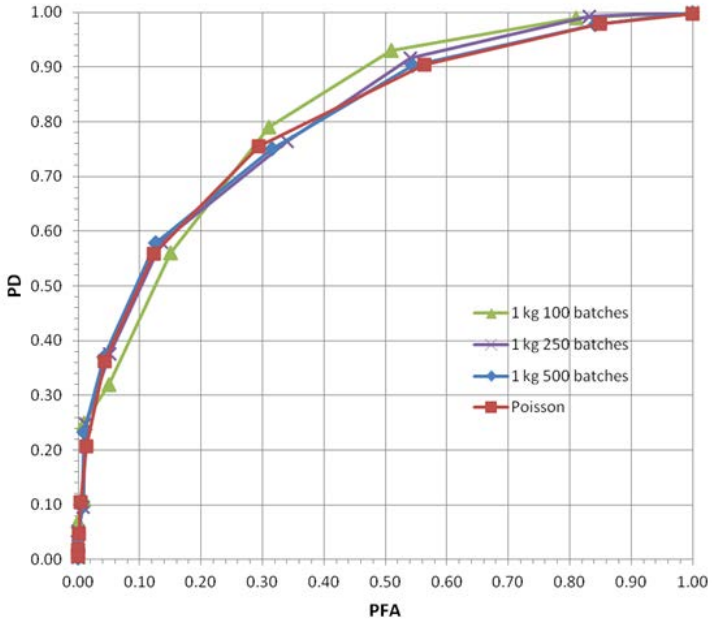

Fig. 48. Approach to Poisson Distribution Neutron ROC 1-kg Pu Bare Ball

It should be noted that the ROC curve presented in Figure 48 utilized a neutron background from the background.dat file and consequently a single deterministic value was utilized. As we have discussed relatively large temporal fluctuations in the background may exist which may actually result in departures from Poisson behavior as shown in Figure 44 C. To simulate this phenomena a probability distribution function must be specified for the background. Otherwise the simulations performed to determine the ROC Curve represent a notional ROC Curve with an assumed mean background signal utilized in the simulation.

A ROC curve can be constructed in MCNP6 with any tally as long as MCNP has a way to simulate the two component signals (Signal, Noise) within a single run.

A common way to construct a ROC curve is to use an F8/pulse height tally (PHT). One can also use the pulse height light (PHL) special tally option to create the pulses and generate a ROC curve. In the example used here, the neutron response of a He-3 detector will be modeled as pulses. The pulses are generated in MCNP using a PHL tally from the charged particles created by the He-3 capture reaction (p-t) or (d-d) are created and deposit energy in the gas.

Before proceeding it should be mentioned that the standard F8 tallies are not appropriate for ^{3}He proportional counters because F8 tallies do not produce reliable spectra when the particles are produced in the same media that ultimately generate the detection signal. The standard F8 tally scores the difference in energy between when a particle enters a material and when it is no longer available for tracking (either because it escaped the cell or was captured while in the cell). If the

particle is created in the cell in which the signal is generated, and doesn't technically "enter" the cell, the F8 tally results will not be accurate.[68]

Consequently, modeling the detector response of ^{3}He involves using the PHL treatment involves converting the energy deposition from the F6 tally into an equivalent amount of light, which can be registered by the F8 tally.[69]

Having laid the groundwork for the MCNP ^{3}He neutron detector, we begin by first modeling all of the desired sources in the input file within a single run. These can include background sources, spontaneous fission sources, decay gamma sources (either SP or ordinary photon distributions), etc. The sources should all have sampling frequencies that reflect the relative intensities for each. Table 10 presents an example MCNP source input used to properly sample a spontaneous fission source, background neutron source as well as a background photon source.

Table 10. MCNP Source for ^{3}He Detector Simulation

```
sdefpar=d1 x=FPAR=d2 y=FPAR=d3 z=FPAR=d4
      cel=FPAR=d5
      wgt=1         $ required for ROC.  will use sampling probability
      loc=37.7 -122.7 0.196 $ SNLL 37.7 N 122.7 W 196m
c
si1 L   -sf   -bn    -bp  $ use -sf, -bn, and -bp to preserve weight
c        sf/total      bn/total      bp/total
sp1   2.20636E-05  2.550005E-01  7.449775E-01  $ 40 kg 97% 2000cm cube
```

The particle is configured as a distribution of spontaneous fission (sf), background neutrons (bn), and background photon (bp). The sampling among them is determined by their relative intensities. The weight of each particle is set to 1.

Once the source is configured, it is necessary to choose the means by which the signal will be distinguished from the background, i.e., noise in the tallies. One option is to use the source itself and mark it as noise or signal. This approach is not ideal, since a background source can create noise directly in the detector or, if amplified by a multiplying media, can become a "signal."

Another way to differentiate the source signal from the background is to apply a flag such as the first fission tally (FFT) special tally treatment. In this way any particle can create a "signal" if it triggers a response—a fission—in the object and the same type of source can contribute to noise if it interacts in the detector without interacting with the object.

In this example, the energy deposited by the charged particles from ^{3}He capture is recorded by the respective F6 tallies. The PHL tally will be used to sum these energies and create pulses from them. The total signal (S+N) is simply all pulses recoded in the detector from sources. This will come from adding all three possible light-ion signals in tallies 6, 16, 26, and 36.

The total signal will be combined with tallies that recorded negative “signal” (-S), tallies 46, 56, 66, and 76. The use of the FFT will separate when fission has occurred in the object. The negative FM multiplier is used to make this (S) into (-S). Note that it is necessary to run MCNP6 with the “fatal” option in order to override the error when using a negative FM value. In this way linear superposition of the total tallies (S+N) and negative signal (-S) will result in the noise (N) tally. This superposition will be done in MCNP in the PHL tally processing. Table 11 presents the construction of the signal+noise as well as the signal tallies.

Table 11. MCNP Tally Construction for ^{3}He Detector

```
c ----> TALLIES
c
c tallies for the PHL
c
c Total signal (S+N)
f6:h  5008
f16:t 5008
f26:d 5008
f36:s 5008

c
c
c Godiva and Godiva+bn to subtract from total signal
f46:h 5008
ft46 FFT
fu46 18 0
fm46 -1.0  $ this will subtract the signal.
c
f56:t 5008
ft56 FFT
fu56 18 0
fm56 -1.0  $ this will subtract the signal.
c
f66:d 5008
ft66 FFT
fu66 18 0
fm66 -1.0  $ this will subtract the signal.
c
f76:s 5008
ft76 FFT
fu76 18 0
fm76 -1.0  $ this will subtract the signal.
```

Once the physics and tallies have been chosen, it is necessary to construct the inputs to the ROC curve. This should consist of the “Signal+Noise” (S+N) and “Noise” (N) inputs.

The inputs to the F8 PHL tally are groups of F6 tallies that are shown in Table 12. The first line represents the total (S+N) tallies, the second line is the addition of (S+N) and (-S) which gives the (N).

Table 12. ^{3}He Construction of PHL Tallies Signal and Background

```
c
c
f8:n 5008
ft8   PHL 3    6 1   16 1   26 1 36 1
          6    6 1   16 1   26 1   46 1   56 1   66 1 76 1
```

Once the tally groups for (S+N) and (N) have been defined, the next step is to specify which energy and tally fluctuation bins will be used to construct the ROC curve. The PHL tally option can be created to include energy bins, including a threshold bin, below which the pulses can be ignored. Here 0.1 MeV is used at the threshold value (t) and the upper value is 1000 to capture all other signals. The (S+N) energy bins will be represented by the energy (e8) bins. The (N) energy bins will be presented by the user (fu8) bins. Each pulse that is scored will be put into one of the four bins based on the magnitude of the two components [(S+N) and (N)]. Table 12 presents the four possible outcomes for the signal plus noise and the noise.

Table 13. Signal and Noise Possible Outcomes for ROC Construction

	Noise (user bins)	
S+N (energy bins)	< t	> t
< t	S is small or zero	Impossible
>t	Signal	Noise

The TF bins are defined for the two ROC signals from which to construct the ROC curve. The first line should represent the S+N, so the counts are summed from both user bins and the second energy bin (sum of second row). The Noise component then is simply the 2nd energy, 2nd user bin alone. The threshold for the detector energy and the TF bins are depicted in Table 14.

Table 14. ^{3}He Detector PHL energy thresholds and tf settings for ROC Curve Generation

```
e8  0.1 1000 (lower and upper thresholds for detection)
fu8 0.1 1000
fq8 e u
tf8   j j 1,2 j j j 2 j
      j j   2 j j j 2 j
c
c
```

The last step in the construction of the ROC is to choose the number of batches to use in the ROC processing and the size of the batch. The batch size should correspond to a typical count time such that the distribution of counts achieved for the batches is identical to the expected count distributions in the detection scenario. In this example, the total emission rate of all sources is 3.831e5 particles/sec (8.44 sf-n/sec, 9.77e4 bn/sec, and 2.85e5 bp/sec). The count time is 100s. So each ROC batch should run 3.831e7 particles. The total number of particles run (nps) will be the product of the size of the batch times the number of batches. In this case, 100 batches of 3.831e7 would yield 3.831e9 total particles. Table 15 presents the ROC parameters.

Table 15. ROC Parameter Settings for 100 seconds and 3.831e5 particles/sec

```
ROC 3.831461e7  100          $ 2000 x 2000
```

Examples of ROC for a select number of objects are presented in Appendix C.

Finally, McKinney has observed through examination of various physics parameters in MCNP associated with the detectability of small quantities of SNM surrounded by a thin lead shield of areal mass 5 g/cm2 with a 3” NaI detector located 50 cm from the object with a 0.1-sec count time with 100 batches.

1) **ECUT parameter should probably be kept at 1 keV**. Significant changes in the PD (i.e., factors of 2) at low PFA values were observed when ECUT was increased to 50 keV in important regions (HEU, HEU shield, detector shield). These changes were even larger when ECUT was increased to 100 keV. There is likely a value between 1 and 50 keV that could be used.
2) **EMAX parameter should probably be placed at 3 GeV** (at least for photon detection). Significant changes in PD occurred at low PFA when EMAX was increased from 1 to 3 GeV. There was little change between 3 GeV and 5 GeV.
3) **No need to add FISSION=p,e or NONFISS=e to the ACT card.** No notable changes to the ROC curves occurred when delayed-betas were included, nor did delayed-gamma production from induced fission have any impact (likely because the number of induced neutron and PN fissions is quite small due to the small SNM utilized).
4) **Detector type is very important.** Changing from a 3” NaI detector to a 12” plastic (BC-416) detector made a notable improvement to the ROC curves as illustrated in Fig. 42.

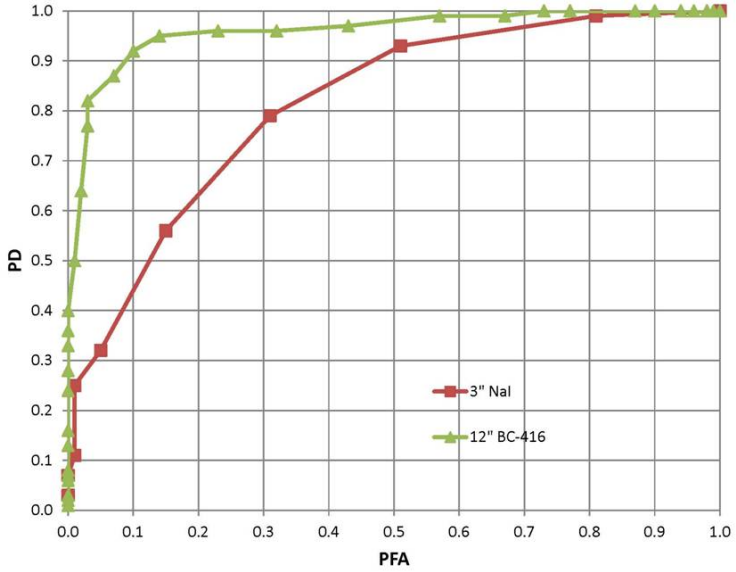

Fig. 49. Demonstration of Sensitivity of ROC to Detector Type for 1 kg HEU both 50 cm from Object with 5 g/cm2 Lead Shielding and 0.1-sec Count Time

7.0 Conclusions

A comprehensive methodology has been presented to describe the use of MCNP6 to model the radiation signatures sources from an object containing SNM. A comprehensive examination of numerous physics issues that arise in the modeling of radiation signatures has been performed. Based on these investigations, choices for the inclusion of appropriate physics, detector tallying, and finally the detectability of objects in the presence of backgrounds, recommendations for MCNP modeling parameters and modeling approaches are presented. Numerous examples of objects and leakages have been provided. Calculations of ROCs have been presented that provide a means of assessing. Finally, radiation signature benchmarking calculations with existing experimental data has begun to validate the methodology presented in this report.

Appendix A

MCNP models for both neutron and photon detectors were developed for use in simulations. The NaI detector is depicted in Fig. A.1.

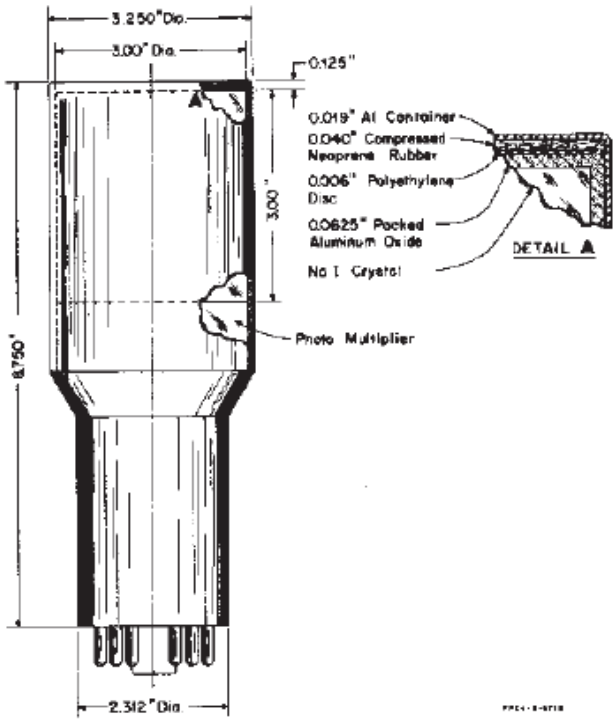

Figure A. 1 Typical NaI detector with PMT

The MCNP model for the NaI detector was modeled from the dimensions and materials given in A.1.[70] The photo multiply tube (PMT) was modeled using a 1 to 1 mixture of SiO_2 and BeO. The volume of the PMT was calculated from Fig A.1 and the density of the mixture was adjusted to obtain the weight of 0.65 kg given for an ORTEC 276L Low-Power Photomultiplier Base. The NaI detector would typically be placed in a lead shield to reduce background in the detector. Figures A.2–5 provide details of the overall NaI detector, a closeup of the NaI crystal, the PMT in conjunction to the NaI crystal, and the PMT. Material definitions are provided in Table A.1.

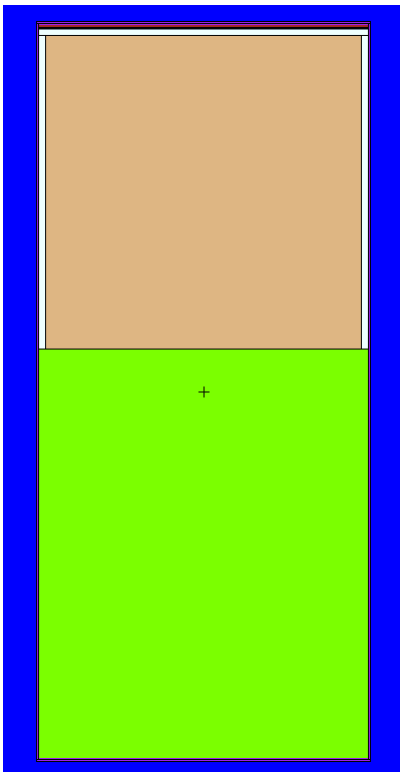

Figure A. 2 NaI Detector

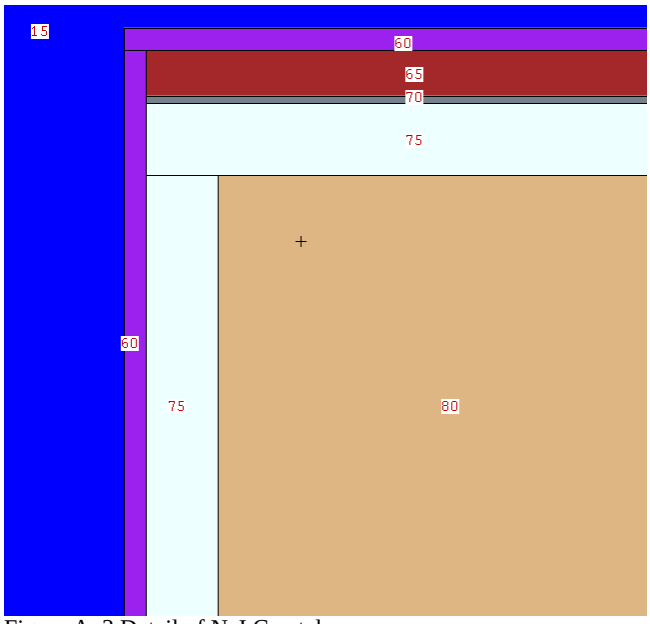

Figure A. 3 Detail of NaI Crystal

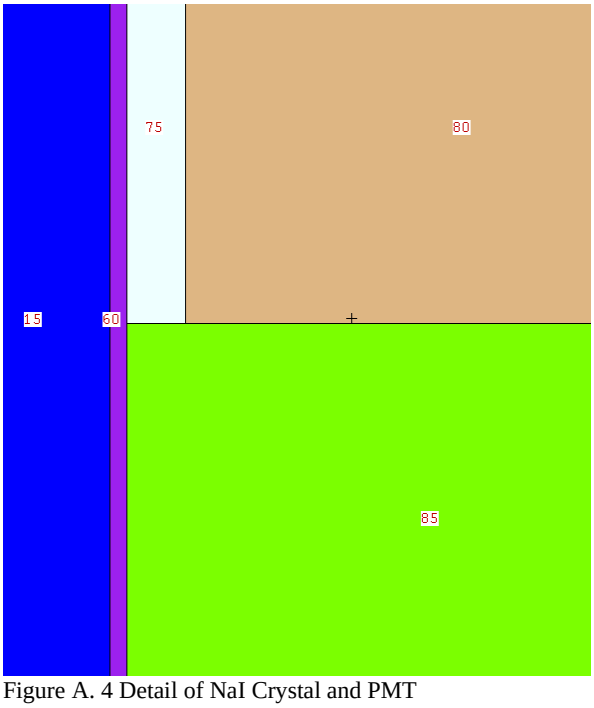

Figure A. 4 Detail of NaI Crystal and PMT

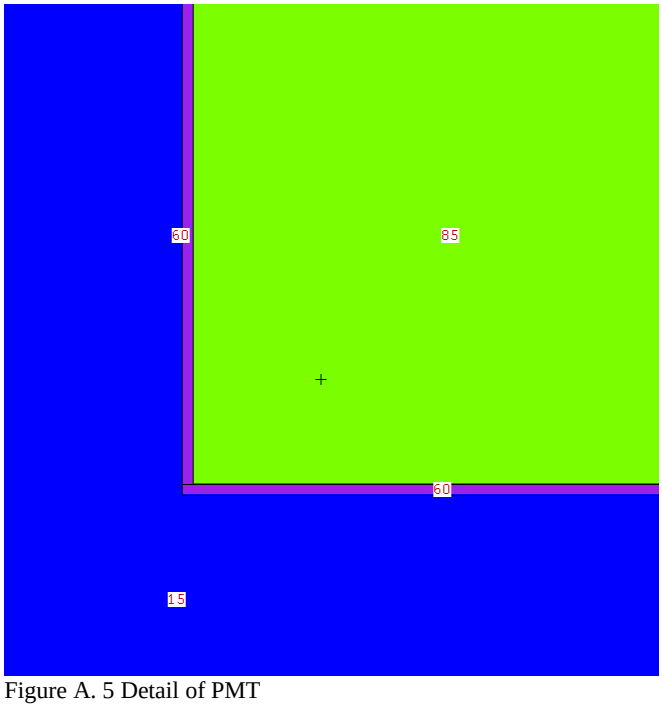

Figure A. 5 Detail of PMT

Table A. 1 Material Composition of NaI Detector

Material Number Identifier	Material
Material 60	Aluminum
Material 65	Neoprene
Material 70	High Density polyethylene
Material 75	Aluminum Oxide
Material 80	NaI
Material 85	1 to 1 mixture of SiO_2 and BeO
Material 90	Lead

A model for a SNAP 3 ^{3}He neutron detector based on Fig. A.6 was developed.[71]

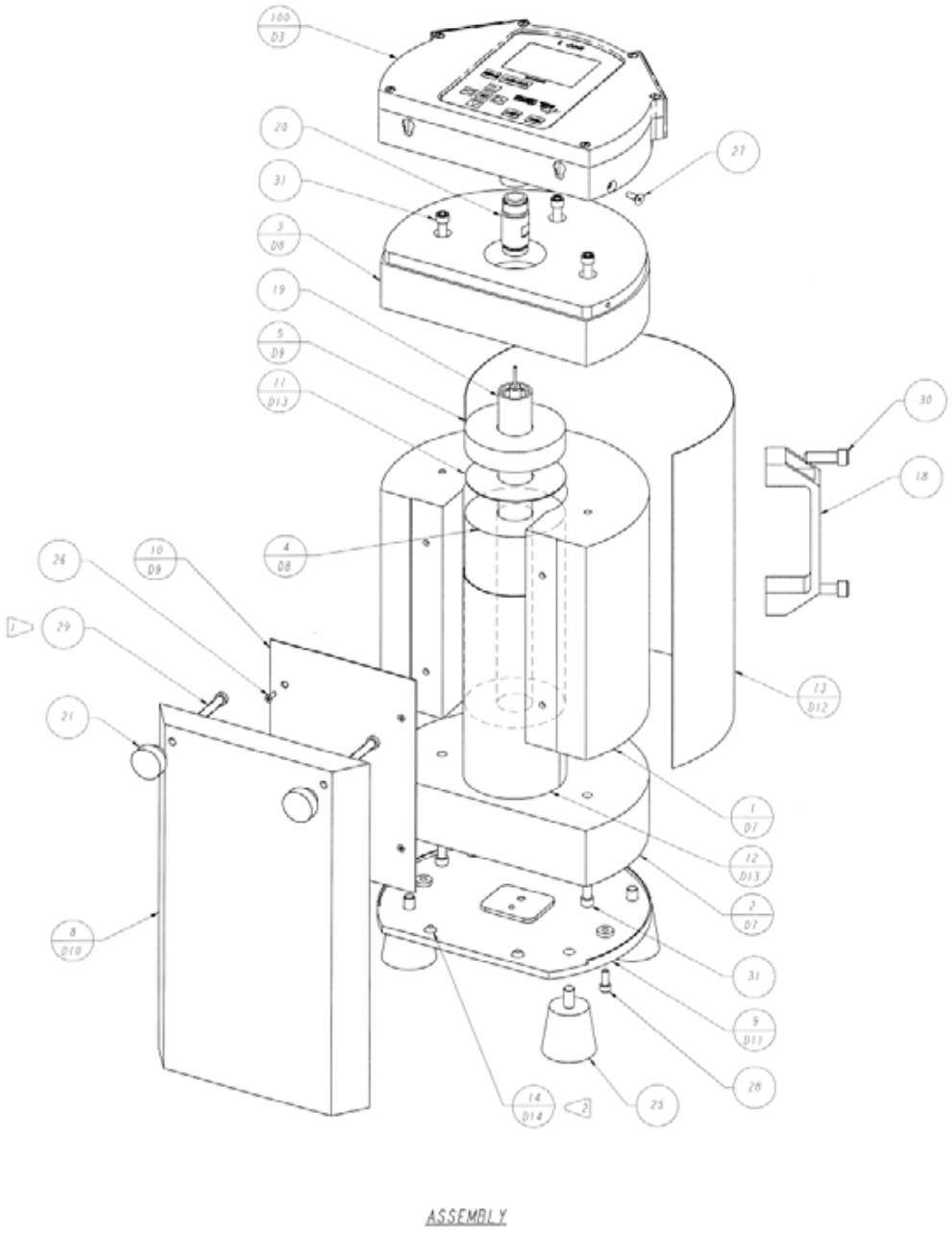

Figure A. 6 Schematic of LANL SNAP-3 Detector (Mattingly, 2009)

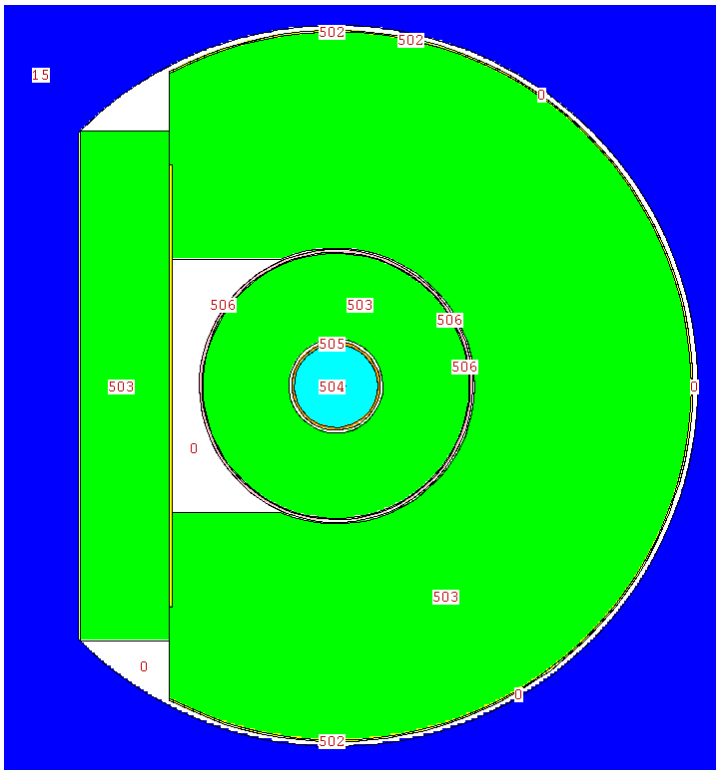

Figure A. 7 SNAP-3 Detector Horizontal Cross Section of MCNP Model

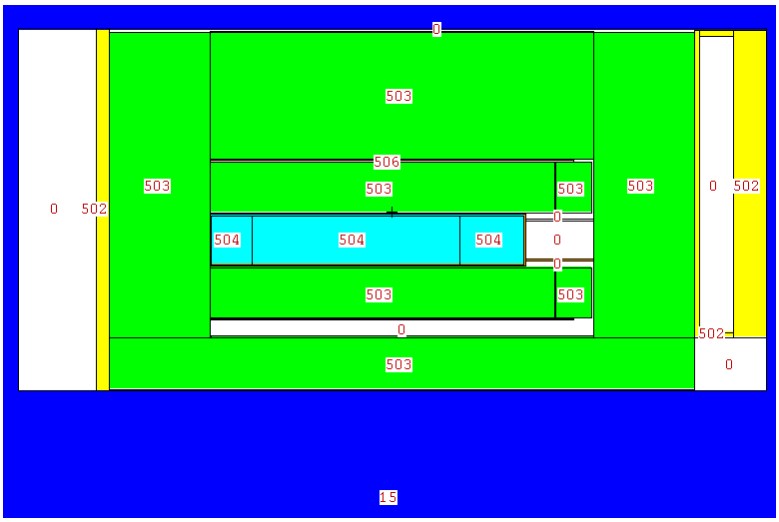

Figure A. 8 SNAP-3 Detector Vertical Cross Section of MCNP Model

Table A. 2 SNAP-3 Detector Materials

Cell Number	Material
15	Air
502	Aluminum
503	Polyethylene
505	Stainless Steel 304
506	Cadmium

8.0 References

[1] Klasky, M., et al., "DNDO Radiation Signature Analysis and Device Mapping Assessment," Los Alamos National Laboratory report LA-CP-14-XX

[2] LLNL Team, Threat Matrix Volume I Government Nuclear Devices," September 28, 2010

[3] LLNL Team, Threat Matrix Volume II Improvised Nuclear Devices," September 28, 2010

[4] Sokkappa, P., et al., "Benchmark Sources for Radiation Detection Architecture Evaluation (revision 3), Lawrence Livermore National Laboratory report UCRL-TR-218277-REV-3 (March 2011).

[5] LANL Program Review Comments, 2014

[6] Hayes, "Preliminary Benchmarking Efforts and MCNP Simulation Results for Homeland Security," DOE/NV/25946-431.

[7] Whalen, P., "MCNP: Photon Benchmark Problems," Los Alamos National Laboratory report LA-12196.

[8] Diago, J., Escuela Tecnica Superior De Ingenieros Industriales Universidad Politecnica devalencia espana "Simulation of detector calibration using MCNP" (November 2005).

[9] Pelowitz, D.B., et al., "MCNP6 User's Manual Version 1.0," Los Alamos National Laboratory report LA-CP-13-00634 (2013).

[10] J.S. Hendricks, G.W. McKinney, H.R. Trellue, J.W. Durkee, T.L. Roberts, H.W. Egdorf, J.P. Finch, M.L. Fensin, M.R. James, D.B. Pelowitz, L.S. Waters, and F.X. Gallmeier, "MCNPX, Version 2.6.A," Los Alamos National Laboratory report LA-UR-05-8225 (2005).

[11] Gwon, C., et al., "Software for the Optimization of Radiation Detectors (SWORD)," Naval Research Laboratory, Physics-Based Modeling in Design & Development for U.S. Defense Conference

[12] Holloway, S., et al., "A Manual for Cinder 2008," Los Alamos National Laboratory report LA-UR-11-00006.

[13]Bell, M., "ORIGEN-The ORNL Isotope Generation and Depletion Code," Oak Ridge National Laboratory report ORNL-4628

[14] BNL National Nuclear Data Center, http://www.nndc.bnl.gov/

[15] Ibid 1

[16] Wilson, W.B., Perry, R.T., Charlton, W.S., Parish, T.A., Estes, G.P., Brown, T.H., Arthur, E.D., Bozoian, M., England, T.R., Madland, D.G., Stewart, J.E., "SOURCES-4A: A Code for Calculating (alpha,n), Spontaneous Fission, and Delayed Neutron Sources and Spectra," Los Alamos National Laboratory report LA-13639-MS (1999).

[17] Shores, E., "Plutonium oxide benchmark problems for the SOURCES code," *Applied Radiation and Isotopes* **62**, 699–704 (2005).

[18] http://www.talys.eu/contact/

[19] Norman, D. et al., "Highly Enriched Uranium (HEU) Detection Options," Los Alamos National
Laboratory report LAUR-14-21979 (2014).

[20] Ibid 19

[21] Keith, R., "Dual Neutral Particle Beam Interrogation of Intermodal Shipping Containers for Special Nuclear Material," thesis, University of New Mexico (May 2013).

[22] Slaughter, D. et al.,"Early Results Utilizing High-Energy Fission Product (Gamma) Rays to Detect Fissionable Material in Cargo," Lawrence Livermore National Laboratory report, UCRL-JRNL-207073.

[23] Hall, J.M., Asztalos, S., Biltoft, P., Church, J., Descalle, M.-A., Luu, T., Manatt, D., Mauger, G., Norman, E., Petersen, D., Pruet, J., Prussin, S., Slaughter, D., "The Nuclear Car Wash: Neutron Interrogation of Cargo Containers to 271 Detect Hidden SNM," *Nuclear Instruments and Methods in Physics Research B*, Vol. 261, pp. 337–340 (2007).
[24] Moss et al., Comparison of Active Interrogation Techniques., *IEEE Transactions on Nuclear Science* **53**, 4 (August 2006).
[25] Fensin, M., McKinney, G., "How to use the MCNP6 Background Source Capability," *Transactions- American Nuclear Society* **109**, 1198.
[26] Ibid 9
[27] Ibid 25
[28] Ibid 25
[29] Thoreson, G., "A General Nuclear Smuggling Scenario Analysis Platform," thesis, University Texas Austin (August 2011)
[30] Ibid 1
[31] Runkle, R., Smith, E., Peurrung, A., "The photon haystack and emerging radiation detection technology", *Journal of Applied Physics* **106**, 2009.
[32] Ennslin, N., et al., "Application Guide to Neutron Multiplicity Counting," Los Alamos National Laboratory report LA-13422-M (November 1998).
[33] McMath, G., Private Communications
[34] Slaughter, D.R., et al., "Preliminary results utilizing high-energy fission product g-rays to detect fissionable material in cargo," *Nuclear Instruments and Methods in Physics Research B* **241**, 777–781 (2005).
[35] Sheu, R.J., "A Study of the Cosmic-ray Neutron Field Near Interfaces," *Nuclear Instruments and Methods A* **476,** 52 (2003).
[36] O'Brien, et al., "Cosmic-Ray Induced Neutron Background Sources and Fluxes for Geometries of Air Over Water, Ground, Iron, and Aluminum," *Journal of Geophysical Research-Space Physics* **83,** 114–120 (1978).
[37] Kouzes, R., et al., "Cosmic-Ray induced Ship-effect Neutron Measurements and Implications for Cargo Scanning at Borders," *Nuclear Instruments and Methods in Physics Research Section A* **587,** 89–100 (2009).
[38] Kouzes, R.T., et al., "Passive Neutron Detection for Interdiction of Nuclear Materials at Borders," *Nuclear Instruments and Methods in Physics Research Section A* **584,** 383–400 (2008).
[39] Medalin, J., "Detection of Nuclear Weapons and Materials: Science, Technologic, Observations," Congressional Research Service, June 2010.
[40]Ibid 39
[41] Knoll, G.F., *Radiation Detection and Measurement* (John Wiley & Sons, Inc., New York, 2000), pp. 406–415.
[42] Ibid 39
[43] Ibid 41
[44] Ibid 39
[45] Ely, et al., *IEEE Trans. Nucl Sci. NS-51* 1672 (2004) .
[46] Ibid 45
[47] Ibid 41
[48] Ibid 41

[49] Ibid 21
[50] Alecksen, T., "Novel Techniques for the Detection and Localization of Attenuated Gamma-Ray Sources," thesis, New Mexico Institute of Mining and Technology
[51] Ibid 50
[52] Ibid 50
[53] Ibid 50
[54] Ibid 1
[55] Ibid 9
[56] Heath, R.L., "Scintillation Spectrometry," Reissue of IDO-16880 2nd Edition-Vol I Rev) Tutorial Text
[57] Mattingly, J., "Polyethylene-Reflected Plutonium Metal Sphere: Subcritical Neutron and Gamma Measurements," Sandia National Laboratories report SAND-2009-5804 Rev 1 (Nov 2009)
[58] Ibid 31
[59] Ibid 31
[60] Ibid 31
[61] Ibid 39
[62] Ibid 39
[63] Ibid 39
[64] Ibid 39
[65] Ibid 39
[66] Verbeke, et al., "*Neutron Correlations in Special Nuclear Materials, Experiments and Simulations*," Lawrence Livermore National Laboratory report UCRL-PROC-231582 (June 2007)
[67] Private communicate with Gregg W. McKinney
[68] Ibid 9
[69] Ibid 9
[70] Ibid 56
[71] Ibid 57